AGU PUBLICATIONS

Paleoceanography

RESEARCH ARTICLE
10.1002/2015PA002905

Key Points:
- Carbon and nitrogen isotopes provide complementary constraints on biologically sequestered carbon
- Preliminary estimates indicate 33–44% (510–670 Pg C) more respired organic carbon in the glacial ocean
- Physical and biological effects contribute 18% (280 Pg C) and 15–26% (230–390 Pg C) to the increased respired carbon storage, respectively

Supporting Information:
- Supporting Information S1

Correspondence to:
A. Schmittner,
aschmitt@coas.oregonstate.edu

Citation:
Schmittner, A., and C. J. Somes (2016), Complementary constraints from carbon (^{13}C) and nitrogen (^{15}N) isotopes on the glacial ocean's soft-tissue biological pump, *Paleoceanography*, *31*, 669–693, doi:10.1002/2015PA002905.

Received 19 NOV 2015
Accepted 21 MAY 2016
Accepted article online 26 MAY 2016
Published online 14 JUN 2016

Complementary constraints from carbon (^{13}C) and nitrogen (^{15}N) isotopes on the glacial ocean's soft-tissue biological pump

A. Schmittner[1] and C. J. Somes[2]

[1]College of Earth, Ocean, and Atmospheric Sciences, Oregon State University, Corvallis, Oregon, USA, [2]GEOMAR, Helmholtz Centre for Ocean Research Kiel, Kiel, Germany

Abstract A three-dimensional, process-based model of the ocean's carbon and nitrogen cycles, including ^{13}C and ^{15}N isotopes, is used to explore effects of idealized changes in the soft-tissue biological pump. Results are presented from one preindustrial control run (piCtrl) and six simulations of the Last Glacial Maximum (LGM) with increasing values of the spatially constant maximum phytoplankton growth rate μ_{max}, which accelerates biological nutrient utilization mimicking iron fertilization. The default LGM simulation, without increasing μ_{max} and with a shallower and weaker Atlantic Meridional Overturning Circulation and increased sea ice cover, leads to 280 Pg more respired organic carbon (C_{org}) storage in the deep ocean with respect to piCtrl. Dissolved oxygen concentrations in the colder glacial thermocline increase, which reduces water column denitrification and, with delay, nitrogen fixation, thus increasing the ocean's fixed nitrogen inventory and decreasing $\delta^{15}N_{NO3}$ almost everywhere. This simulation already fits sediment reconstructions of carbon and nitrogen isotopes relatively well, but it overestimates deep ocean $\delta^{13}C_{DIC}$ and underestimates $\delta^{15}N_{NO3}$ at high latitudes. Increasing μ_{max} enhances C_{org} and lowers deep ocean $\delta^{13}C_{DIC}$, improving the agreement with sediment data. In the model's Antarctic and North Pacific Oceans modest increases in μ_{max} result in higher $\delta^{15}N_{NO3}$ due to enhanced local nutrient utilization, improving the agreement with reconstructions there. Models with moderately increased μ_{max} fit both isotope data best, whereas large increases in nutrient utilization are inconsistent with nitrogen isotopes although they still fit the carbon isotopes reasonably well. The best fitting models reproduce major features of the glacial $\delta^{13}C_{DIC}$, $\delta^{15}N$, and oxygen reconstructions while simulating increased C_{org} by 510–670 Pg compared with the preindustrial ocean. These results are consistent with the idea that the soft-tissue pump was more efficient during the LGM. Both circulation and biological nutrient utilization could contribute. However, these conclusions are preliminary given our idealized experiments, which do not consider changes in benthic denitrification and spatially inhomogenous changes in aeolian iron fluxes. The analysis illustrates interactions between the carbon and nitrogen cycles as well as the complementary constraints provided by their isotopes. Whereas carbon isotopes are sensitive to circulation changes and indicate well the three-dimensional C_{org} distribution, nitrogen isotopes are more sensitive to biological nutrient utilization.

1. Introduction

Understanding the glacial ocean's carbon cycle remains a major challenge in paleoceanography and at the heart of the problem to explain the low atmospheric CO_2 concentration, which was ~190 ppm during the Last Glacial Maximum (LGM; 26–19 ka B.P.) and thus ~90 ppm lower than that during the preindustrial late Holocene [*Marcott et al.*, 2014; *Parrenin et al.*, 2013; *Petit et al.*, 1999]. Since biologically available (fixed) nitrogen, such as nitrate (NO_3), is a major nutritional element required for phytoplankton growth, the nitrogen and carbon cycles are linked through the biological pump [*Redfield*, 1958]. The biological pump refers to processes of biological uptake of carbon and other elements at the surface, sinking, remineralization, and sequestration at depths [*Volk and Hoffert*, 1985]. It can be separated into a soft-tissue component associated with organic matter and the hard-tissue pump associated with calcium carbonate ($CaCO_3$) cycling. Here we focus on the dominant soft-tissue pump.

In the following we will use the terms "efficiency of the soft-tissue pump" and "remineralized organic carbon storage" synonymously, although strictly speaking the efficiency of the soft-tissue pump may be best defined as the ratio P_{org}/P_{tot} of the whole ocean inventory of phosphate from the remineralization of organic matter over that of total phosphate, whereas remineralized organic carbon storage C_{org} refers to the whole ocean

inventory of dissolved inorganic carbon (DIC) from the remineralization of organic matter. Both are linked $C_{org} = R_{C:P}P_{org}$ through the stoichiometric ratio of phosphorous to carbon in organic matter (here we use $R_{C:P} = 106$) [*Redfield*, 1958] and the assumption of a constant P_{tot}, although it has been suggested that P_{tot} may have varied over glacial-interglacial time scales [*Wallmann*, 2014] and that $R_{C:P}$ is not strictly constant [*Weber and Deutsch*, 2010; *Galbraith and Martiny*, 2015].

Changes in the nitrogen cycle have been hypothesized to impact the soft-tissue pump. A substantial increase of the fixed nitrogen inventory of the ocean during the LGM due to either diminished sinks (water column denitrification, WCD, and benthic denitrification, BD, which occurs in sediments) or enhanced sources (nitrogen fixation, NF), would have made the soft-tissue pump more efficient [*Archer et al.*, 2000; *Broecker and Henderson*, 1998; *Eugster et al.*, 2013; *Falkowski*, 1997; *McElroy*, 1983]. More effective utilization of surface nutrients through iron fertilization or increased stratification has also been suggested as a mechanism to increase the efficiency of the soft-tissue pump [*Knox and McElroy*, 1984; *Martin*, 1990; *Martinez-Garcia et al.*, 2014; *Sarmiento and Toggweiler*, 1984; *Sigman and Boyle*, 2000]. Others have inferred enhanced carbon storage in the abyssal ocean due to more sluggish flow and/or reduced vertical mixing [*Sarnthein et al.*, 2013; *Skinner et al.*, 2010; *Toggweiler*, 1999], deeper remineralization of organic matter [*Matsumoto et al.*, 2007], or reduced burial of organic matter in shallow sediments [*Wallmann et al.*, 2016].

All of those hypotheses have in common the idea that C_{org} was increased in the glacial ocean consistent with qualitative reconstructions of dissolved oxygen concentrations [*Galbraith and Jaccard*, 2015; *Jaccard and Galbraith*, 2011]. However, quantitative estimates of biological carbon storage are still lacking. It also remains unclear how much weight is carried by each of the above mentioned processes. Here we combine a process-based, three-dimensional model of ocean biogeochemistry and isotopes with observations from glacial sediments to quantify biological carbon storage and aid identification of the processes responsible.

Increased C_{org} would also likely have increased whole ocean alkalinity through sediment interactions [*Boyle*, 1988; *Brovkin et al.*, 2007; *Hain et al.*, 2010; *Ikeda and Tajika*, 2003; *Omta et al.*, 2013; *Sigman et al.*, 2010; *Toggweiler*, 1999]. Bottom waters would have become more corrosive with respect to $CaCO_3$ buried in surface sediments. Dissolution of sedimentary $CaCO_3$ would have increased whole ocean alkalinity and carbon, thus acting as a positive feedback, a process often referred to as $CaCO_3$ compensation [*Broecker and Peng*, 1987].

Isotope ratios of both carbon ($^{13}R_C = {}^{13}C/{}^{12}C$) and nitrogen ($^{15}R_N = {}^{15}N/{}^{14}N$), usually reported as delta values ($\delta^{13}C = {}^{13}R_C/{}^{13}R_{C,std} - 1$; $\delta^{15}N = {}^{15}R_N/{}^{15}R_{N,std} - 1$), are used routinely in paleoceanography to infer changes in physical and biological processes related to ocean carbon storage. $\delta^{13}C$ measured on shells of benthic foraminifera has been interpreted as changes in ocean circulation and the accumulation of C_{org} in the deep ocean [*Broecker*, 1982; *Curry and Oppo*, 2005; *Shackleton et al.*, 1992]. $\delta^{15}N$ measured on bulk organic matter or specific compounds has been used to reconstruct changes in subpolar nutrient utilization, WCD, and NF [*Altabet et al.*, 2002; *Ren et al.*, 2009; *Studer et al.*, 2015]. However, both isotopes are influenced by a variety of processes including transport by the circulation and mixing [*Schmittner et al.*, 2013; *Somes et al.*, 2010], which complicates their interpretations based on individual sediment cores alone.

The distribution of $\delta^{13}C$ in DIC ($\delta^{13}C_{DIC}$) in the contemporary ocean is dominated by fractionation during photosynthesis. Phytoplankton assimilate ^{12}C faster than ^{13}C, which leads to lower $\delta^{13}C$ of organic matter relative to its source $\delta^{13}C_{DIC}$ and higher $\delta^{13}C_{DIC}$ in the remaining surface water DIC. Remineralization of isotopically light organic matter at depth decreases $\delta^{13}C_{DIC}$ there. On the other hand temperature-dependent fractionation during air-sea gas exchange tends to increase $\delta^{13}C_{DIC}$ of cold and deep water, thus opposing the trends generated by biology. However, since air-sea gas exchange is slow, the effect of biology dominates the modern $\delta^{13}C_{DIC}$ distribution. The $CaCO_3$ cycle does not significantly affect $\delta^{13}C_{DIC}$ since fractionation during $CaCO_3$ production is small. Lower whole ocean $\delta^{13}C_{DIC}$ in the glacial is typically interpreted as a transfer of isotopically light organic carbon from land [*Shackleton*, 1977]. Simple budget equations for ^{12}C and ^{13}C (see supporting information) indicate an increase of the ocean's carbon inventory by ~300–700 Pg C [*Brovkin et al.*, 2002; *Ciais et al.*, 2012; *Peterson et al.*, 2014].

$\delta^{15}N_{NO3}$ is strongly affected by WCD, which preferentially removes ^{14}N thus increasing $\delta^{15}N_{NO3}$ of the remaining nitrate [*Cline and Kaplan*, 1975]. NF introduces isotopically relatively light nitrogen, thereby decreasing $\delta^{15}N_{NO3}$ in areas where it occurs [*Minagawa and Wada*, 1986]. Phytoplankton take up ^{14}N faster

than ^{15}N, which increases $\delta^{15}N_{NO3}$ of the remaining water and has a large effect in subtropical gyres where NF is not compensating [*Wada*, 1980].

Previous modeling studies have been performed mostly with much more idealized physical models such as box or zonally averaged models [*Brovkin et al.*, 2007; *Bouttes et al.*, 2011; *Eugster et al.*, 2013; *Hain et al.*, 2010; *Köhler et al.*, 2010] and/or considered either carbon or nitrogen isotopes separately, but not both simultaneously [*Tagliabue et al.*, 2009]. Although useful, simplified physical models are prone to limitations in their physics and comparisons with spatially distributed observations are difficult, whereas models that use only one isotope miss potentially important observational constraints.

Here we explore the complementary constraints on biologically sequestered carbon provided by ^{13}C and ^{15}N isotopes, for the first time, in a well-tested, three-dimensional, coupled model of ocean circulation and biogeochemistry. The model results will be compared directly to the reconstructions at the locations where they were taken. However, rather than aiming at realistic simulations, here we restrict ourselves with simplified experiments of the LGM in which the efficiency of the soft-tissue pump is altered in an idealized manner, but the glacial circulation is kept the same to investigate carbon-nitrogen cycle interactions and constraints provided by their isotopes. The goal is to pave the way toward a more quantitative understanding of the glacial ocean's carbon cycle.

2. Materials and Methods

2.1. Model Description

The Model of Ocean Biogeochemistry and Isotopes (MOBI 1.5) is coupled online to the global University of Victoria (UVic) Earth System Climate Model version 2.9. The UVic model consists of a three-dimensional ocean general circulation model at coarse resolution ($1.8 \times 3.6°$, 19 vertical levels), a one-layer energy-moisture balance atmospheric component, a dynamic/thermodynamic sea ice model [*Weaver et al.*, 1999], and a land surface/dynamic vegetation module [*Meissner et al.*, 2003]. The idealized atmospheric component allows simulations of multiple millennia in a computationally efficient manner. However, it comes with the caveat that atmospheric processes are simplified, such that winds used in air-sea exchange and moisture transport as well as clouds are prescribed at a repeated but fixed seasonal cycle estimated from a modern climate reanalysis [*Kalnay et al.*, 1996]. The model physics used here is identical to that of model PD (present day) of *Schmittner et al.* [2015]. In the following we will refer to this model as the preindustrial control (*piCtrl*).

The biogeochemistry is identical to that used by *Schmittner and Lund* [2015]. MOBI is unique in that it includes both nitrogen [*Somes et al.*, 2013, 2010] and carbon [*Schmittner et al.*, 2013] isotopes as well as the more standard cycles of nitrogen, phosphorous, carbon, alkalinity, oxygen, and dissolved organic matter [*Somes and Oschlies*, 2015] and simple plankton ecosystem dynamics (Figure 1). The model's present-day simulations of both physical and biogeochemical fields, including the isotopes, have been extensively tested and carefully compared and found to be consistent with observations, at least at large spatial scales, notwithstanding biases as described in the above references.

The model version used here does not include carbon exchange with sediments. Fluxes of organic matter and $CaCO_3$ that would enter the sediments are remineralized in the bottom box. Therefore, whole ocean inventories of phosphorous and alkalinity are conserved in the model and effects of $CaCO_3$ compensation are not included. Simulated changes in preformed and total carbon will thus not be realistic, because those quantities would have been influenced by whole ocean alkalinity changes. However, biologically sequestered organic carbon is not impacted by alkalinity and therefore its simulation will be more reliable.

In the following we briefly summarize the carbon and nitrogen cycles and their isotopes as represented in the model. For full details we refer the reader to the above references. ^{13}C and ^{15}N are modeled in all carbon and nitrogen compartments of the model, almost tripling the number of prognostic biogeochemical tracers.

The oceanic carbon cycle is governed by air-sea gas exchange of CO_2, which fractionates isotopes such that surface ocean DIC is ~2‰, approximately 8.5‰ enriched compared to the atmosphere $\delta^{13}C_{CO2} = -6.5‰$. However, fractionation during air-sea gas exchange is temperature dependent such that colder waters have higher $\delta^{13}C_{DIC}$. Uptake of DIC by phytoplankton fractionates by about $\varepsilon_P = -20‰$ and depends on the pCO_2 of surface waters. Remineralization of the isotopically light organic carbon in the subsurface increases DIC

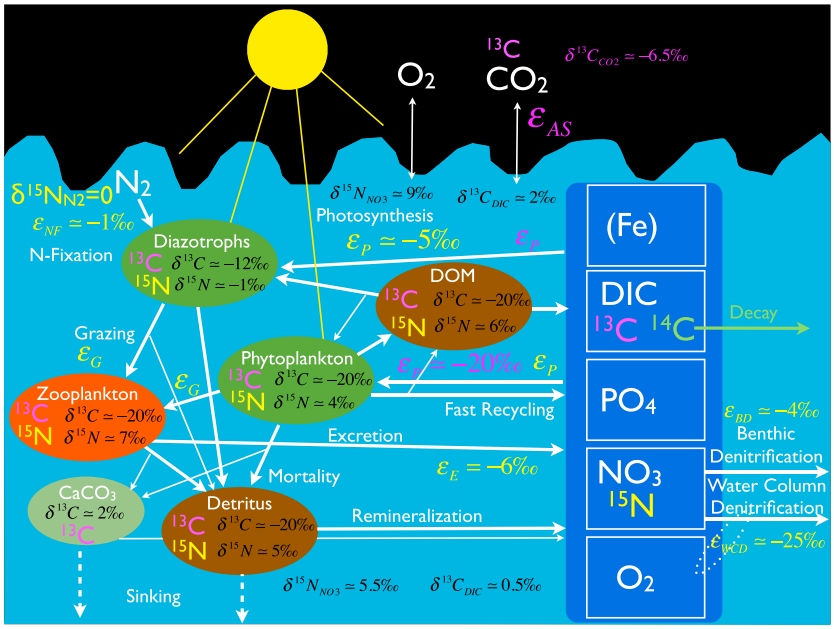

Figure 1. Schematic diagram of MOBI showing biological compartments on the left and inorganic compartments on the right. Two types of phytoplankton, diazotrophs and other phytoplankton, and one type of zooplankton describe the living biota in fixed elemental ratios N:P:C. Many of the biological fluxes such as photosynthesis, fast recycling, and remineralization depend exponentially on temperature. Nonliving organic matter is represented by sinking particulate detritus and nonsinking dissolved organic matter (DOM), which has varying elemental ratios. $CaCO_3$ is not a prognostic variable, but its production at the surface is instantaneously redistributed using an *e*-folding depth of 4 km. Iron (Fe), which limits growth of both diazotrophs and phytoplankton, is not a prognostic variable, but its concentrations in the top three layers are prescribed from a model that includes iron cycling. ^{15}N (yellow) and ^{13}C (purple) are tracked in all compartments that contain nitrogen or carbon, respectively. Fractionation factors are indicated as epsilon values with the corresponding fluxes, and typical (preanthropogenic) delta values are noted within the various compartments. For the dissolved inorganic compartments delta values are indicated for the surface and deep ocean separately.

and decreases $\delta^{13}C_{DIC}$ there. Biological production of $CaCO_3$ at the surface and dissolution at depths affect DIC and alkalinity in the model, but its effect on carbon isotopes is negligible.

The nitrogen inventory is controlled by a balance of NF and denitrification, which is modeled both in the water column and in the sediments. Calculation of BD considers subgrid-scale bathymetry and depends on organic carbon fluxes, bottom water, oxygen, and nitrate [*Bohlen et al.*, 2012]. BD fractionates isotopes only weakly consistent with observations, which suggest that it typically utilizes the majority of NO_3 in sediment pore waters [*Lehmann et al.*, 2007]. WCD occurs only in suboxic waters with dissolved oxygen concentrations below 5 μM. It fractionates strongly ($\varepsilon_{WCD} = -25‰$) by preferentially removing the light ^{14}N isotope, thus leaving behind enriched $\delta^{15}N_{NO3}$. Nitrogen is fixed by diazotrophs, which have lower growth rates than regular phytoplankton but do not rely on nitrate because they are able to convert dinitrogen gas (N_2) into organic matter. NF fractionates weakly and adds isotopically light ($\delta^{15}N = -1‰$) nitrogen to the ocean, which has a mean value of $\delta^{15}N_{NO3} \cong 5.5‰$.

Isotopic fractionation also occurs during internal nitrogen cycling. Preferential uptake of isotopically light dissolved inorganic nitrogen (DIN) during photosynthesis increases the $\delta^{15}N_{NO3}$ of the remaining nitrate by about $\varepsilon_P = -5‰$. This leads to relatively high $\delta^{15}N_{NO3}$ values in the DIN-depleted subtropical gyres in the absence of NF. Zooplankton excrete preferentially the light isotope, which increases the $\delta^{15}N$ of their organic matter.

2.2. Setup of LGM Experiments

The experimental setup of the LGM simulations is simplified but considers major forcings such as the presence of ice sheets, atmospheric CO_2 concentrations, and changes in Earth's orbital parameters [*Schmittner et al.*, 2015]. For all LGM simulations presented in this paper we use identical physics, namely, those of model

Table 1. Summary of Numerical Experiments, Global Inventories, and Fluxes[a]

	μ_{max} (day^{-1})	C_O (Pg C)	C_{org} (Pg C)	EP (Pg C/yr)	PP (Pg C/yr)	N_O (PgN)	NF (TgN/yr)	WCD (TgN/yr)	BD (TgN/yr)
piCtrl	0.6	37,358	1,522	7.6	65	620	141	69	72
LGM0.6	0.6	36,523	1,803	6.8	52	645	83	20	64
LGM0.7	0.7	36,842	2,030	7.1	49	646	122	57	66
LGM0.8	0.8	37,052	2,197	7.2	49	630	161	96	68
LGM0.9	0.9	37,193	2,326	7.3	49	607	206	139	71
LGM1.0	1.0	37,291	2,427	7.4	50	575	253	184	74
LGM1.2	1.2	37,407	2,561	7.5	52	508	334	258	83

[a]Columns from left to right: abbreviated experiment name, maximum phytoplankton growth rate, inventories of total ocean carbon (C_O) and respired organic carbon (C_{org}), carbon fluxes of export production (EP) and primary production (PP), the inventory of total bioavailable nitrogen (N_O), fluxes of nitrogen fixation (NF), water column denitrification (WCD), and benthic denitrification (BD).

LGM PDmix described in the supporting information and Figure S3 of *Schmittner et al.* [2015]. All simulations use present-day winds, clouds, and tidal energy input. The change in global mean salinity of about 1 (salinity is unitless, but values are comparable to units used earlier such as g/kg or practical salinity unit) due to lower sea level has not been included in the model simulations since the dynamical effects would be minimal. Lower sea levels during the LGM also likely caused reduced benthic denitrification [*Christensen*, 1994]. In our LGM experiments, however, the bathymetry and the subgrid-scale bathymetry used in the calculation of benthic denitrification are unchanged from piCtrl and thus do not consider the effects of sea level lowering. Neither considered are changes in river drainage directions.

Iron fertilization of the glacial ocean due to higher dust fluxes has been implicated in glacial ocean carbon drawdown [*Martin*, 1990]. However, estimates of soluble, bioavailable iron fluxes from dust to the surface ocean have large uncertainties due to variations in sources, chemical transformations during transport, and iron speciation [*Albani et al.*, 2014; *Lambert et al.*, 2015; *Mahowald et al.*, 2009, 2006]. Moreover, the marine iron cycle is complex and the response to increased aeolian iron fluxes depends strongly on model assumptions [*Parek et al.*, 2004]. Rather than exploring these complex uncertainties, here we opt for a simpler approach by increasing the maximum growth rates of phytoplankton μ_{max} in a spatially uniform manner. Increased μ_{max} and higher bioavailable iron concentrations both affect the biological pump in a similar way by accelerating rates of inorganic nutrient and carbon uptake by phytoplankton in the euphotic zone. The standard LGM simulation is repeated six times by increasing μ_{max} incrementally from its standard value of 0.6 day^{-1} used in piCtrl to 1.2 day^{-1}. The experiments are labeled *LGM0.6*, *LGM0.7*, *LGM0.8*, *LGM0.9*, *LGM1.0*, and *LGM1.2*, where the number corresponds to the value of μ_{max} (Table 1). Diazotroph's maximum growth rates are $0.08 \times \mu_{max}$, where 0.08 is the handicap factor, and thus increase in the same proportion as those for other phytoplankton. It is important to keep in mind that these experiments are idealized since aeolian iron flux changes likely led to a spatially inhomogenous increases in phytoplankton growth rates, whereas here we apply a constant increase of μ_{max} everywhere. Note that actual simulated changes in phytoplankton growth rates will not be uniform since they also depend on temperature and nutrient limitation.

Atmospheric boundary conditions for CO_2 and $\delta^{13}C_{CO2}$ are set to 280 ppm and -6.5‰ for the piCtrl and 185 ppm and -6.5‰ for the LGM simulations, respectively, consistent with ice core measurements [*Marcott et al.*, 2014; *Schmitt et al.*, 2012]. Both piCtrl and the LGM simulations were all initialized from previous preindustrial and LGM states with a similar model around the arbitrary model year 4500 and then integrated for another 5000 years. Whereas the circulation and physical properties are in equilibrium at that time, some of the biogeochemical tracers still show minor drifts as will be discussed later. Most results will be presented from the last 100 years of those simulations.

2.3. Model Analysis

In order to better understand simulated changes in the carbon cycle, we decompose $DIC = C_{pre} + C_{rem}$ into preformed and remineralized contributions, with $C_{rem} = C_{CaCO3} + C_{org}$, where C_{CaCO3} and C_{org} represent DIC from the dissolution of $CaCO_3$ and the remineralization of organic matter, respectively. In the corresponding

decomposition for $\delta^{13}C_{DIC} \approx \delta^{13}C_{pre} + \delta^{13}C_{org}$ contributions from $CaCO_3$ can be neglected. See *Schmittner et al.* [2013] for details of the calculations.

2.4. Sedimentary Reconstructions

LGM carbon isotopes will be compared to a recently published synthesis of 434 epibenthic (cibicides) foraminiferal data [*Peterson et al.*, 2014], assuming that they represent $\delta^{13}C_{DIC}$ [*Duplessy et al.*, 1984], although it is likely that foraminiferal calcite $\delta^{13}C$ is influenced to a lesser degree by other factors [*Hesse et al.*, 2014; *Spero et al.*, 1997]. Modeled nitrogen isotopes will be compared to 50 data from the recent synthesis of reconstructions from the Nitrogen Cycling in the Oceans Past and Present (NICOPP) group [*Galbraith et al.*, 2013] for which LGM − late Holocene differences could be computed. These data, based on bulk organic nitrogen measurements, were corrected for a depth-dependent diagenetic effect by subtracting 0.9‰/km [*Robinson et al.*, 2012]. We have added one data point from diatom bound measurements [*Studer et al.*, 2015] and four data points from foram bound measurements [*Martinez-Garcia et al.*, 2014; *Ren et al.*, 2012, 2009; *Straub et al.*, 2013], which were not corrected for diagenesis, adding up to a total number of 55.

Both $\delta^{13}C$ and $\delta^{15}N$ reconstructions were mapped onto the model grid for comparison with the model results. In order to maximize the available data pairs, model results were extrapolated modestly by averaging neighboring ocean grid points to fill an adjacent land grid point both horizontally and vertically. Averaging observations onto the model grid reduces the number of data points to $N = 51$ for $\delta^{15}N$ and to $N = 365$ for $\delta^{13}C$, because several observations may fall into one model grid box.

3. Results

The analysis focusses on carbon and nitrogen isotopes and related biogeochemical fields and covers pertinent physical changes as briefly as possible.

3.1. Physics

Despite the simplified experimental setup, the model reproduces major physical characteristics of the LGM climate. Global average surface air temperature is 4.3°C colder in the LGM run, and global sea ice cover is with $3.8 \times 10^{13}\,m^2$ much larger than that of the piCtrl run ($2.2 \times 10^{13}\,m^2$), consistent with observations [*Annan and Hargreaves*, 2013; *Roche et al.*, 2012]. The top two panels of Figure S3 of *Schmittner et al.* [2015] show that in this LGM simulation the Atlantic Meridional Overturning Circulation (AMOC) is shallower and weaker (11 Sv versus 17 Sv) than that in piCtrl.

The global mean radiocarbon age ($C^{14}age = -\ln(r^{14})/(\ln(2)/(5730\ a))$, where $r^{14} = \Delta^{14}C/1000 + 1$ and 5730 a is the radiocarbon half-life, increases from 1410 (1650) years in piCtrl to 1940 (2260) years in LGM (numbers in brackets denote averages below 2 km depth). The corresponding $\Delta^{14}C$ values are −155‰ (−180‰) and −207‰ (−239‰). The simulated increase of 600 years below 2 km depth is in good agreement with recent estimates based on sediment reconstructions [*Sarnthein et al.*, 2013] and a combination of sediment data with an inverse model (L. Skinner, personal communication, 2015). The remaining drift at model year 9800 is very small (+0.4 C^{14} years per 100 model years below 2 km depth). Bottom waters in the LGM simulation are colder everywhere and saltier almost everywhere except for the North Atlantic, where they are fresher compared with piCtrl (Figure S1 in the supporting information) due to the shoaling and weakening of the AMOC (since Antarctic Bottom Water (AABW) is fresher than North Atlantic Deep Water (NADW) in the model). The simulated pattern of salinity changes indicates enhanced brine rejection from intensified sea ice formation in the Weddell Sea, consistent with earlier results [*Schmittner*, 2003]. In most locations the simulated changes in bottom water properties are at least qualitatively consistent with observations [*Adkins et al.*, 2002; *Insua et al.*, 2014]. However, the salinification of bottom waters in the Atlantic sector of the Southern Ocean and in the Pacific is underestimated by the model and in the northwest Atlantic the model predicts fresher bottom water, whereas the reconstructions indicate saltier conditions. The disagreements in the South Atlantic and Pacific may indicate that Antarctic Bottom Water in the model is not salty enough and that the deep ocean in general may be not as stratified in the model as it was in reality, or it may indicate issues in the pore water-based reconstructions [*Miller et al.*, 2015; *Wunsch*, 2016].

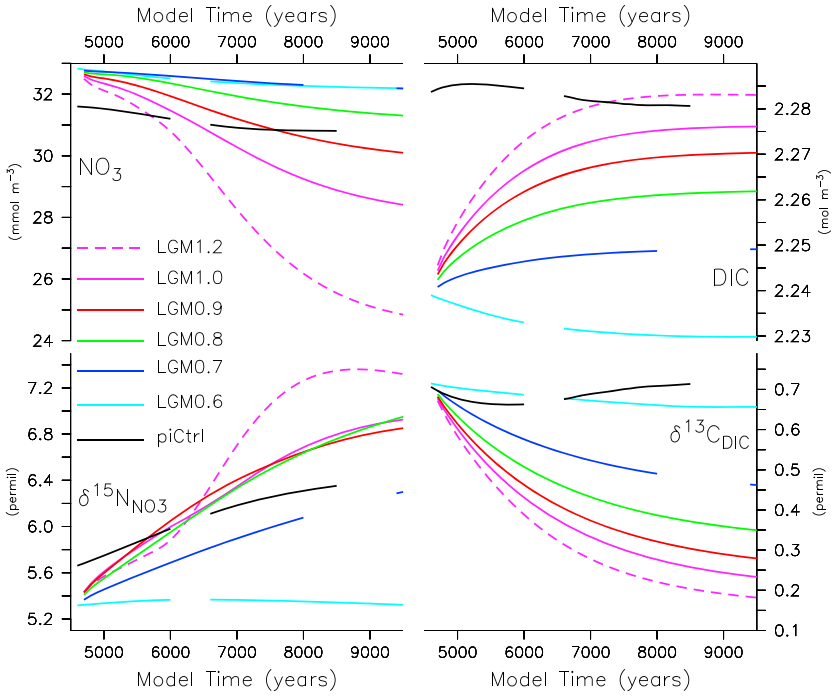

Figure 2. Time series of global mean quantities during model spin-up for six different LGM models (colors) and the preindustrial control run (black). Model time is arbitrary. Gaps in the lines for models piCtrl, LGM0.6 (between years 6000 and 6600 for both), and LGM0.7 (between years 8000 and 9400) indicate lost data.

3.2. Biogeochemistry

Discussion of the biogeochemistry starts with global mean changes in carbon and fixed nitrogen storage and their isotopes, followed by vertical distributions of horizontally averaged quantities, before discussions of the full three-dimensional distributions.

3.2.1. Global Mean Carbon and Nitrogen Inventories and Their Isotopes

Figure 2 shows the long equilibration times for the nitrogen and carbon inventories as well as for their isotopes. The total carbon content of the ocean C_O, which can be approximated by its mean DIC concentration (see supporting information and Table 1), increases for most simulations, except for piCtrl and LGM0.6, for which it stays relatively constant. All LGM simulations equilibrate at lower carbon inventories than piCtrl except LGM1.2, which approaches similar but slightly larger values. However, these changes are not realistic due to our neglect of sediment interactions, which leads to near-constant global mean alkalinity. Small variations in whole ocean alkalinity in the order of O(0.01 mol/m^3), from 2.415 in piCtrl, via 2.420 in LGM0.6, to 2.428 in LGM1.2 (mol/m^3), between the simulations are due to changes in nitrate sources and sinks [see *Schmittner et al.*, 2008, equation 2].

All LGM simulations store more respired organic carbon than piCtrl (Table 1). In the default LGM0.6 case C_{org} is increased by about 280 Pg C or roughly 18%, whereas models with larger μ_{max} show larger increases by ~510 (33%), 670 (44%), 800 (53%), 910 (59%), and 1040 Pg C (68%) for LGM0.7 through LGM1.2, respectively. Between the LGM experiments relative changes in C_{org} are similar to but slightly smaller than relative changes in μ_{max}. The ratio of relative changes is $(C_{org,LGM0.7}/C_{org,LGM0.6})/(0.7/0.6) = 0.96$ at small μ_{max} and decreases slightly at higher μ_{max} $(C_{org,LGM1.2}/C_{org,LGM1.0})/(1.2/1.0) = 0.88$. Thus, although not quite linear, changing μ_{max} is an efficient way to change C_{org} in the model. The same conclusion holds if the efficiency of the soft-tissue pump, expressed as P_{org}/P_{tot}, is considered, which increases from 41% in piCtrl to 48% in LGM0.6, 54% in LGM0.7, 59% in LGM0.8, 62% in LGM0.9, 65% in LGM1.0, and 68% in LGM1.2.

C_{pre} is reduced by 970 to 1100 Pg in the LGM simulations compared with piCtrl or by about 1/30th of the preindustrial carbon inventory due to the decrease in prescribed atmospheric CO_2 from 280 to 180 ppm.

(Dissolved organic carbon C_{DOC} changes between the experiments are less than 20 Pg and thus negligible.) This is consistent with a Revelle factor $RF_0 = [(dCO_2/CO_2)/(d\mathrm{DIC}/\mathrm{DIC})]_{\mathrm{ALK=const.}}$ of about 10 [*Zeebe and Wolf-Gladrow*, 2001] and a decrease in atmospheric CO_2 by about $dCO_2/CO_2 = 1/3$.

Export production (EP, the sinking of detritus across 130 m) and primary production (PP, from phytoplankton and diazotrophs) decrease from piCtrl to LGM0.6 (Table 1). Export production, which is strongly controlled by the circulation, is reduced by 10%, most likely due to the weaker AMOC and associated diminished upwelling of nutrients [*Schmittner*, 2005]. Primary production is reduced more strongly (by 20%) since many biological rates in the model depend exponentially on temperature. This slows nutrient uptake and recycling rates in the colder glacial euphotic zone and leads to smaller values of PP and community phytoplankton growth rates $\mu = \mathrm{PP}/(\mathrm{P}+\mathrm{D})$, where P and D are phytoplankton and diazotroph biomass, respectively. Averaged globally over the top 130 m, mμ is smaller in LGM0.6 (0.165 day^{-1}) compared with piCtrl (0.177 day^{-1}). Perhaps counterintuitively, μ decreases (to 0.142 day^{-1} for LGM1.2) for models with higher μ_{max} due to decreasing surface nutrient concentrations.

Global mean $\delta^{13}C_{DIC}$ decreases in all simulations, except in piCtrl and LGM0.6, for which it stays relatively constant around 0.7‰. Models with higher μ_{max} drift toward lower values. The relationship between $\delta^{13}C_{DIC}$ and DIC is monotonic for all LGM models, with higher DIC corresponding to lower $\delta^{13}C_{DIC}$ and an approximate change of 0.1 mol C m^{-3}/‰ (or $\partial\Delta C_O/\partial\Delta\delta_O \cong$ 1600 Pg/‰; see supporting information). However, this relationship does not extend to piCtrl, which has both highest DIC and $\delta^{13}C_{DIC}$, because of different atmospheric boundary conditions.

The fixed nitrogen inventory, which can be approximated by the global mean nitrate or dissolved inorganic nitrogen (DIN) concentration, shows a slow decrease from initial values of 32–33 μM in all LGM models, whereas for piCtrl it stays close to 31 μM consistent with modern observations [*Somes et al.*, 2013]. In models LGM0.6 and LGM0.7 the drift is minimal and values stay above 32 μM. In contrast, models LGM1.0 and LGM1.2 show a strong decrease to ~28 and ~25 μM, which corresponds to 7 and 18% decline of N_O. LGM models with only slightly increased values of μ_{max} stay above piCtrl, whereas models LGM0.9 through LGM1.2 equilibrate at lower nitrate inventories. Due to the neglect of changes in BD, all our LGM nitrate values are presumably biased low.

Global mean $\delta^{15}N_{NO3}$, which is determined by a balance of the rates and isotope effects of NF, WCD, and BD [*Brandes and Devol*, 2002; *Somes et al.*, 2013; *DeVries et al.*, 2013], stabilizes around 6.3‰ in piCtrl, thus overestimating modern observations by ~1‰ due to too low BD, which is a common problem in coarse resolution models that do not resolve well coastal processes. In model LGM0.6 global mean $\delta^{15}N_{NO3}$ approaches 5.3‰, about 1‰ lower than piCtrl due to decreased WCD. In the other LGM experiments increases in μ_{max} lead to more WCD and higher global mean $\delta^{15}N_{NO3}$. However, models LGM0.8, LGM0.9, and LGM1.0 all show a similar increase in global mean $\delta^{15}N_{NO3}$ in contrast to their different WCD rates and evolutions of NO_3. Utilization of nitrate in suboxic zones dilutes the effect of WCD on the global mean $\delta^{15}N_{NO3}$, which reduces the sensitivity of global mean $\delta^{15}N_{NO3}$ to the balance between WCD and BD [*Deutsch et al.*, 2004; *Somes et al.*, 2013]. In LGM1.2, the suboxic zones expand through large regions of the North Pacific further increasing global mean $\delta^{15}N_{NO3}$. This indicates that although there is a tendency for models with lower nitrate inventories to have higher global mean $\delta^{15}N_{NO3}$, the relationship is not perfectly monotonic, perhaps because of the complexities of the processes involved, such as the volume of suboxic water and dilution effect. The dilution effect and nitrate utilization in the model's suboxic zones may be overestimated, which would add uncertainty to estimates of past denitrification rates. In model piCtrl a few model grid points show nitrate values between 5 and 10 mmol m^{-3} (Figure S2), which is lower than observed in the modern ocean. However, its mean nitrate concentration in the suboxic zone ($O_2 < 10$ mmol/m^3) is 31 mmol m^{-3}, not much lower than observed (33.5 mmol m^{-3}) [*Somes et al.*, 2013]. In model LGM0.6 this value increases to 36 mmol m^{-3}, as does the minimum nitrate concentration (Figure S2), whereas models with higher μ_{max} show lower values (29 and 24 mmol m^{-3} for LGM0.8 and LGM1.2, respectively). In model LGM1.2 a large number of grid points have very low nitrate concentrations in its large suboxic zones (Figure S2). We will see below that this model is inconsistent with reconstructions.

3.2.2. Vertical Distributions

Global mean vertical profiles of DIC are similar for piCtrl and LGM0.6, except that LGM0.6 values are shifted lower by about 0.05 mol m^{-3} (Figure 3), consistent with the reduced atmospheric CO_2 boundary condition. In contrast, surface $\delta^{13}C_{DIC}$ is similar for all model simulations reflecting identical atmospheric $\delta^{13}C_{CO2}$.

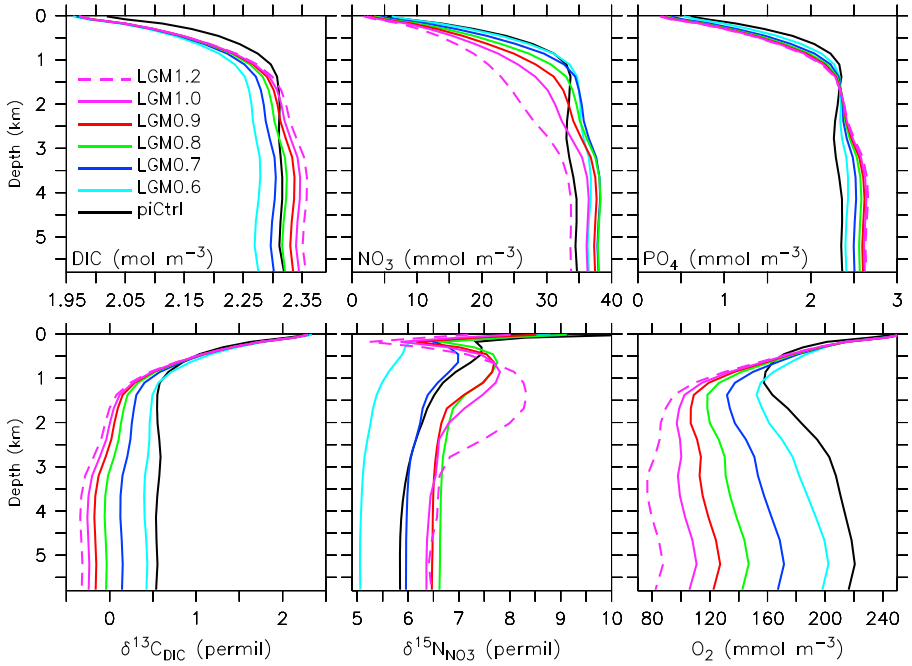

Figure 3. Globally horizontally averaged vertical profiles as a function of depth (m). Colors indicate different model simulations as in Figure 2.

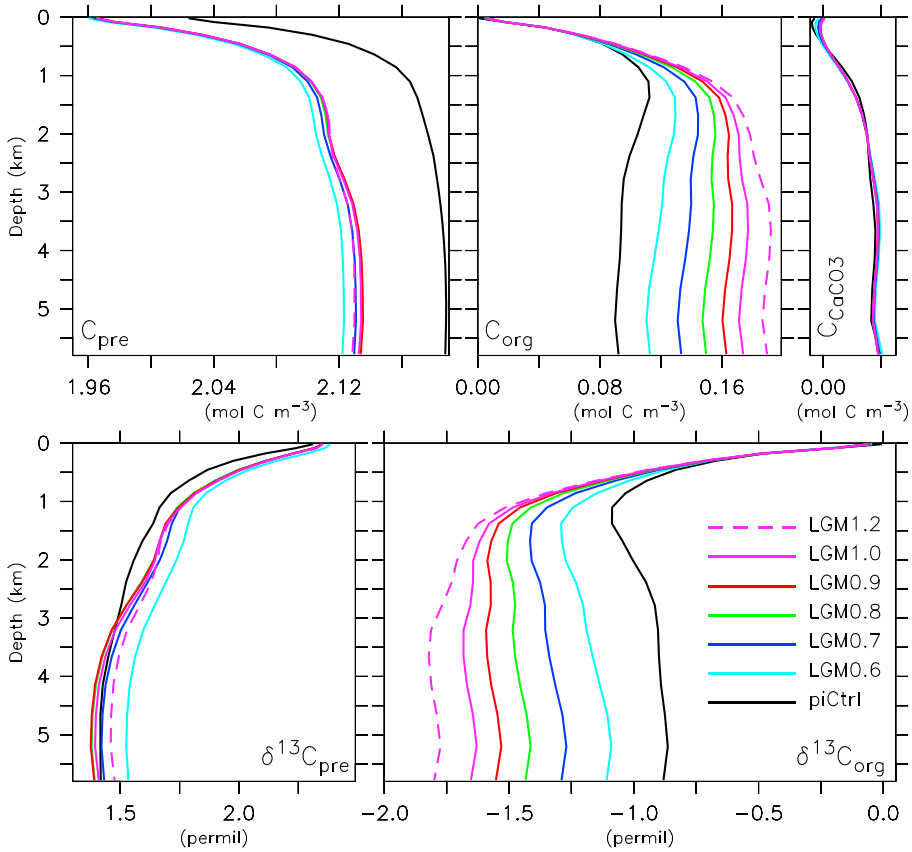

Figure 4. As in Figure 3 but for (top row) DIC and (bottom row) $\delta^{13}C_{DIC}$ decompositions into the effects of preformed (C_{pre}), respired organic (C_{org}) carbon, and the carbonate pump (C_{CaCO3}, top right). For $\delta^{13}C_{DIC}$ the effects of the carbonate pump are negligible and therefore not shown. Horizontal axis ranges are drawn approximately to scale.

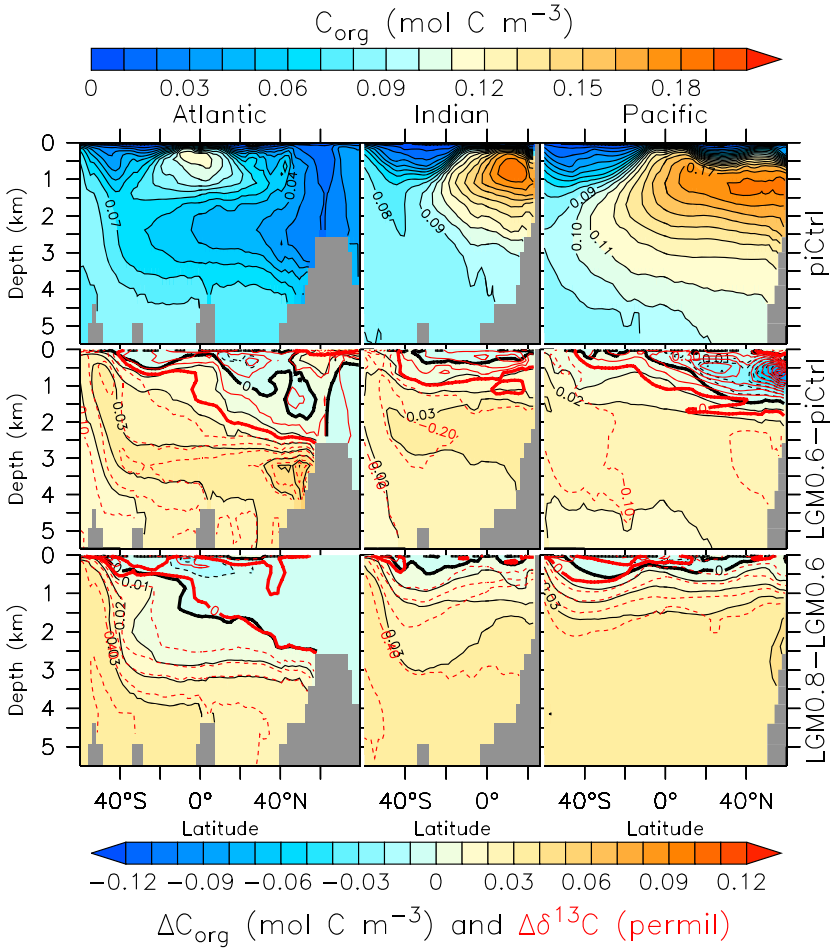

Figure 5. (top row) Zonally averaged concentrations of C_{org} in model piCtrl in the (left) Atlantic, (middle) Indian, and (right) Pacific Oceans (top color scale). (middle row) As in Figure 5 (top row) but differences ΔC_{org} between models LGM0.6–piCtrl, illustrating effects of physics (bottom color scale). Red contour lines show differences in $\delta^{13}C_{DIC}$ between the same models. (bottom row) As in Figure 5 (middle row) but for models LGM0.8–LGM0.6 illustrating effects of biology.

Whereas surface nitrate and phosphate concentrations are similar in models piCtrl and LGM0.6, they decrease for models with higher μ_{max} due to more efficient nutrient uptake. The increased efficiency of the soft-tissue pump in these models results in higher deep ocean PO_4 and larger vertical phosphate gradients, since global mean PO_4 is conserved. In contrast, deep ocean nitrate concentrations increase for moderately higher μ_{max} but decrease for large μ_{max}, reflecting enhanced WCD (Table 1).

Increasing the efficiency of the soft-tissue pump leads to more export production, more remineralization of particulate organic matter in the deep ocean, which increases oxygen consumption and decreases oxygen concentrations there (lower right panel in Figure 3). In the upper ocean, on the other hand, oxygen concentrations are higher in all LGM simulations than in piCtrl, due to increased oxygen solubility at colder temperatures [*Meissner et al.*, 2005]. This pattern is consistent with a recent synthesis of qualitative oxygen changes between the LGM and the early Holocene [*Jaccard and Galbraith*, 2011; *Galbraith and Jaccard*, 2015].

In model LGM0.6 a better oxygenated thermocline shrinks the suboxic water volume and decreases WCD (Table 1), thus lowering global mean $\delta^{15}N_{NO3}$. However, decreasing oxygen concentrations in the deep ocean and thermocline in models with higher μ_{max} lead to a growing volume of suboxic water and more WCD. During the model spin-up this causes an imbalance in the global fixed nitrogen budget such that the nitrate inventory declines and $\delta^{15}N_{NO3}$ increases (Figure 2).

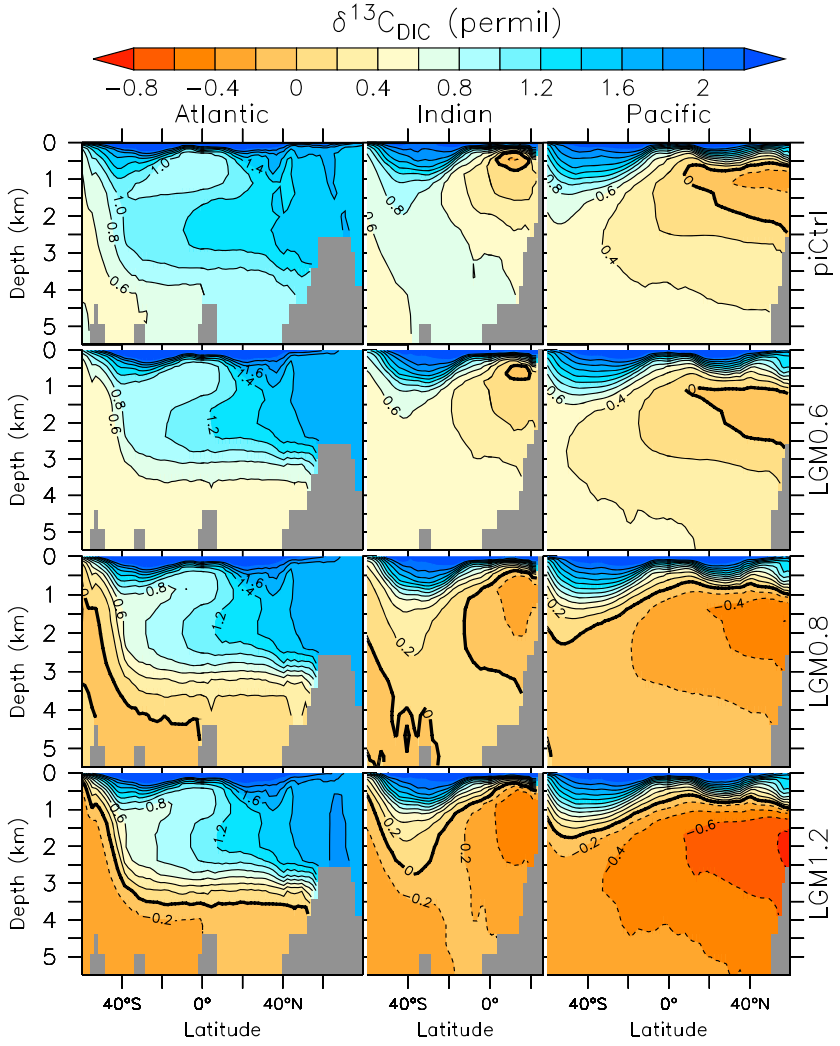

Figure 6. Zonally averaged $\delta^{13}C_{DIC}$ in the (left) Atlantic, (middle) Indian, and (left) Pacific Oceans for different model simulations as indicated at the right margin.

3.2.3. Carbon Cycle

Figure 4 shows that changes in the $CaCO_3$ pump are negligible. Lower atmospheric CO_2 decreases C_{pre} by 0.06–0.07 mol m^{-3} in LGM0.6 compared with piCtrl. LGM0.6 shows increased values of C_{org} in the deep ocean. The effects of larger μ_{max} are expressed in further increases in C_{org} there, whereas they do not affect C_{pre} much. Abyssal ocean C_{org} concentrations in LGM1.2 are about twice those of piCtrl.

Figure 5 illustrates that C_{org} increases between LGM0.6 and piCtrl show distinct maxima at middepths in all ocean basins. The largest increase of ~0.05 mol C m^{-3} is found in the North Atlantic between 3 and 4 km depths, indicating that the shoaling and weakening of North Atlantic Deep Water plays an important role there. The amplitude of the middepths maxima decreases into the Indian Ocean (0.03 mol C m^{-3}) and farther into the Pacific (0.02 mol C m^{-3}). This pattern, tracing the path of NADW flow into the Indian and Pacific oceans, indicates that the weakening and shoaling of the AMOC is important. However, at this point we cannot exclude other mechanisms such as increased sea ice cover or biological effects such as increased fixed nitrogen inventory or increases in remineralization depths due to cooling. Additional sensitivity experiments, which are beyond the scope of this paper, would be needed for a more definitive attribution. Decreases in C_{org} in the North Pacific are caused by decreases in stratification there.

In contrast, increases in μ_{max}, as illustrated in Figure 5 by the differences between LGM0.8 and LGM0.6, induce bottom intensified maxima in ΔC_{org}. These contrasting patterns suggest that different mechanisms

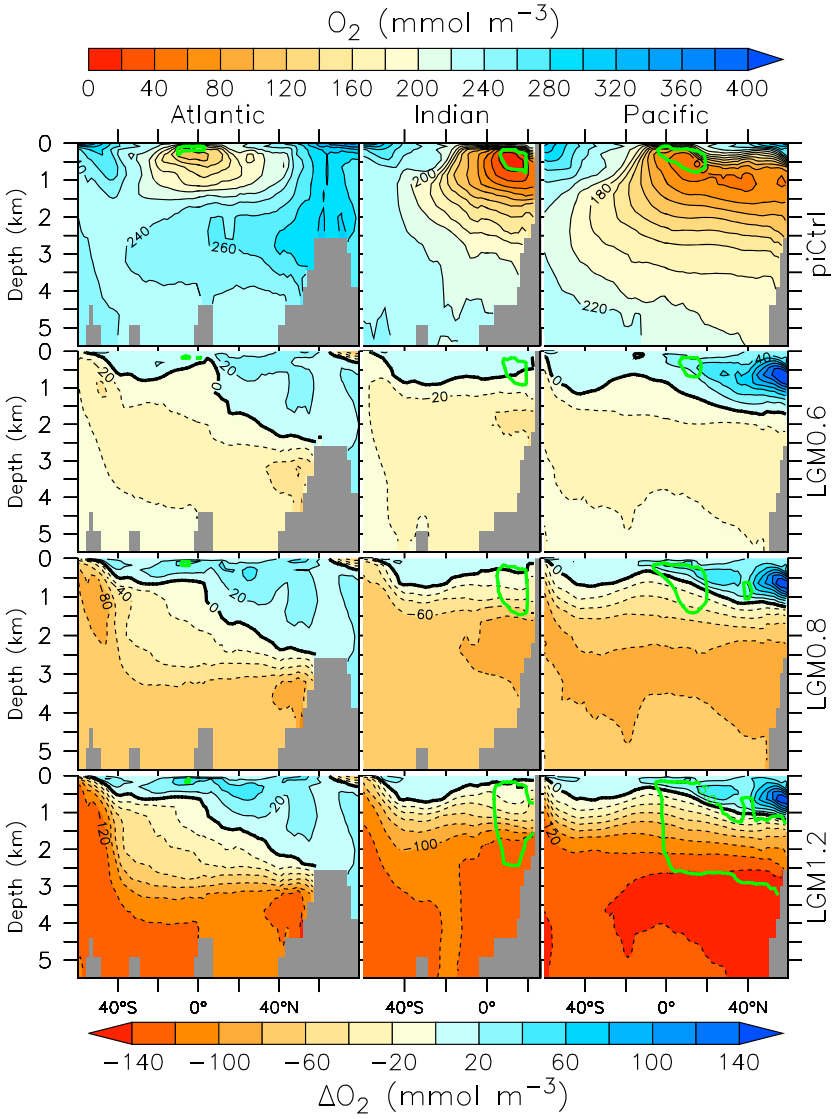

Figure 7. Zonally averaged dissolved oxygen concentrations for (first row) model piCtrl (top color bar) in the (left) Atlantic, (middle) Indian, and (right) Pacific. (second to fourth rows) Oxygen changes (LGM–piCtrl; bottom color bar) for three models as indicated at the right margin. Green contour lines indicate the extent of the suboxic water volume calculated as the 5 μM zonal minimum in oxygen.

can be identified by different distributions of ΔC_{org}. Changes in $\delta^{13}C_{DIC}$ are of opposite sign but very similar in pattern to those in C_{org} between these experiments, and they are highly anticorrelated ($R = -0.89$ for LGM0.6-piCtrl; $R = -0.97$ for LGM0.8-LGM0.6). This suggests that different mechanisms influencing the soft-tissue pump can be identified using deep ocean $\delta^{13}C_{DIC}$ reconstructions. On the other hand, the two ΔC_{org} patterns are correlated ($R = 0.57$) and thus not completely independent from each other, indicating that it may be challenging to separate different mechanisms with sparse $\delta^{13}C_{DIC}$ coverage from paleoceanographic data. This is where independent constraints from nitrogen isotopes may be useful.

3.2.4. Carbon Isotopes

Figure 4 shows that $\delta^{13}C_{pre}$ is increased in LGM0.6 compared to piCtrl by ~0.1‰ despite identical atmospheric $\delta^{13}C_{CO2}$. The reason for this increase is mostly due to temperature-dependent fractionation during air-sea gas exchange. If the surface ocean was in equilibrium with the atmosphere, a 1.8°C cooling, which is the global mean temperature change in the model, would cause a 0.18‰ increase in $\delta^{13}C_{DIC}$ [*Broecker and Maier-Reimer*, 1992]. However, lower atmospheric CO_2 increases the equilibration time of surface

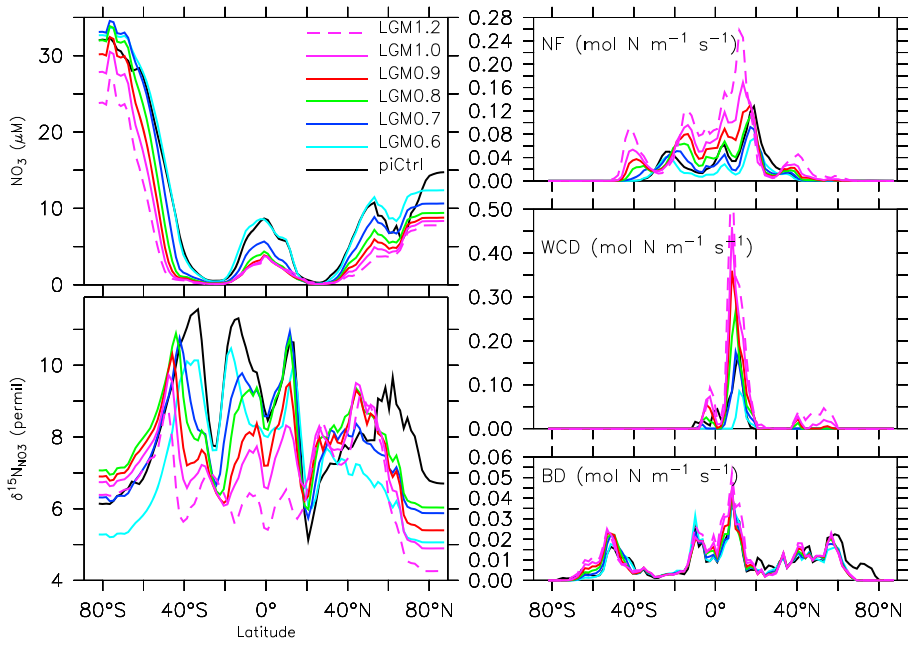

Figure 8. Zonally averaged concentrations of (top left) surface nitrate, (bottom left) $\delta^{15}N_{NO3}$, (top right) vertically integrated nitrogen fixation, (middle right) vertically integrated water column denitrification, and (bottom right) benthic denitrification.

$\delta^{13}C_{DIC}$, which decreases deep ocean $\delta^{13}C_{pre}$ values by about 0.1‰ [*Galbraith et al.*, 2015], countering about half of the temperature effect.

Increasing μ_{max} strongly decreases $\delta^{13}C_{org}$ in the deep ocean. This leads to lower $\delta^{13}C_{DIC}$ at high-latitude surface waters, where deep isopycnals outcrop, and thus decreases $\delta^{13}C_{pre}$ somewhat. But changes in $\delta^{13}C_{pre}$ between the different LGM experiments are much smaller than those for $\delta^{13}C_{org}$.

Zonally averaged $\delta^{13}C_{DIC}$ distributions are quite similar in models piCtrl and LGM0.6 (Figure 6). The most noticeable difference between the two is in the deep Atlantic, where increased invasion of AABW and shoaling of NADW in LGM0.6 decrease $\delta^{13}C_{DIC}$ values consistent with previous interpretations of sediment data [*Curry and Oppo*, 2005; *Gebbie*, 2014]. In the northern North Atlantic $\delta^{13}C_{DIC}$ values increase presumably due to the shoaling of NADW. Both of these changes enhance vertical gradients in the deep Atlantic. In models piCtrl and LGM0.6 only the far North Pacific and a small region in the northern Indian Ocean thermocline show negative values. Increasing μ_{max} reduces deep ocean $\delta^{13}C_{DIC}$ such that in LGM0.8 the entire deep Pacific and large volumes of the deep Indian and South Atlantic Oceans become negative. This tendency intensifies in LGM1.2, for which $\delta^{13}C_{DIC}$ values in the North Pacific become as low as -0.8‰ and the entire deep Indian Ocean as well as the abyssal Atlantic show negative values.

3.2.5. Oxygen

Dissolved oxygen concentrations decrease in the deep ocean in model LGM0.6 compared with piCtrl due to the shoaling and weakening of NADW, which decreases the oxygen supply and increases the accumulated oxygen loss due to respiration of organic matter (Figure 7). In contrast, oxygen concentrations in the thermocline increase presumably due to increased solubility of oxygen in colder water. Ventilation of intermediate waters in the North Pacific is enhanced further, increasing oxygen supply there. Since suboxic zones are located mainly in these thermocline regions where oxygen increases, the volume of suboxic waters is smaller in LGM0.6 compared with piCtrl.

However, increasing μ_{max} decreases oxygen concentrations strongly in the deep and poorly ventilated intermediate ocean thus swelling suboxia there. In model LGM1.2 this effect is so dramatic that suboxic conditions extend throughout much of the North Pacific Ocean between 1 and 3 km depths strongly increasing WCD, a scenario ruled out by sedimentary oxygen reconstructions [*Jaccard and Galbraith*, 2011].

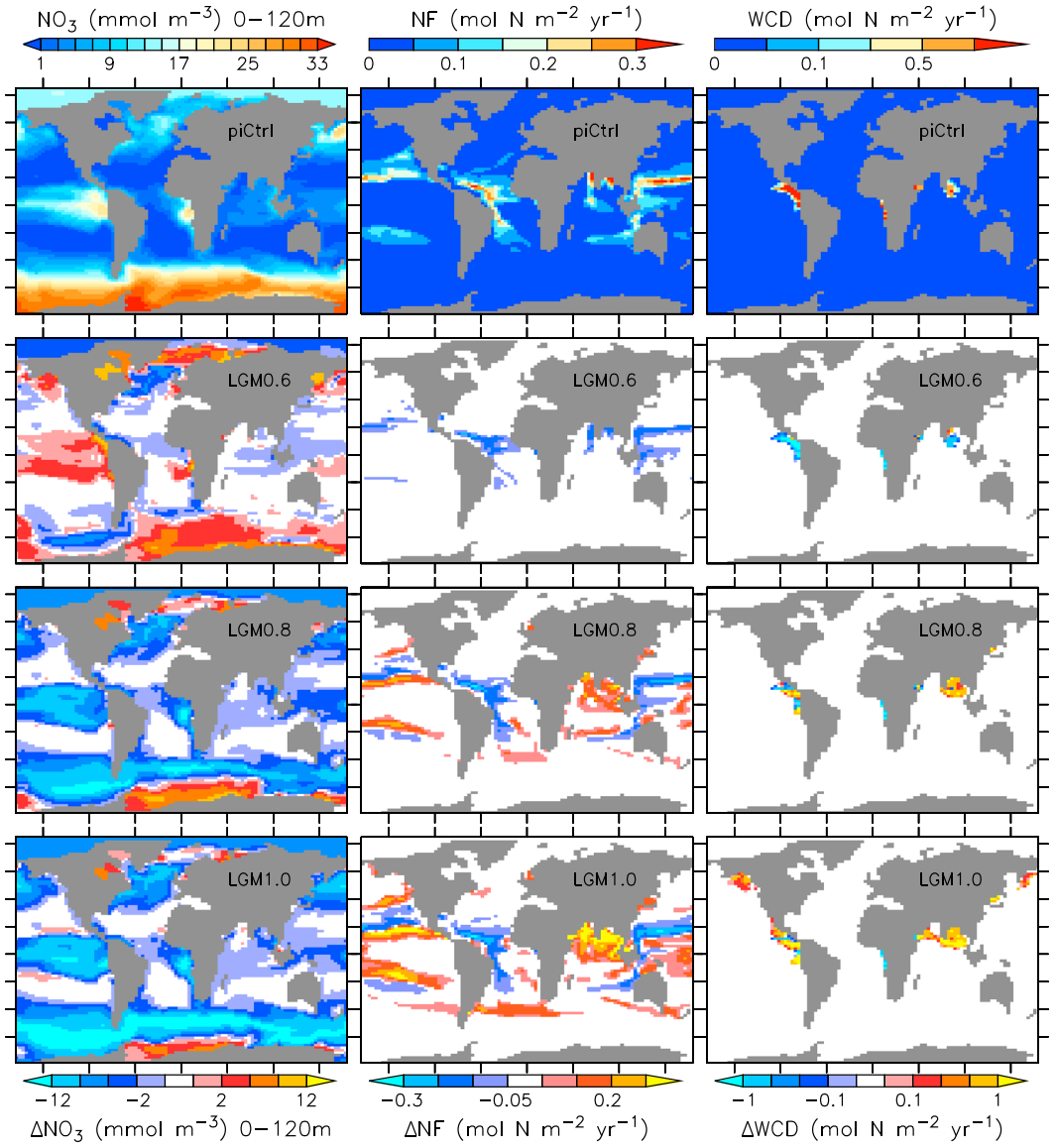

Figure 9. Maps of (left) surface (0–120 m) nitrate, (middle) nitrogen fixation, and (right) water column denitrification from four different models. (first row) Absolute values from piCtrl (top color scales). (second to fourth rows) Changes with respect to piCtrl from models LGM0.6, LGM0.8, and LGM1.0 (bottom color scales). Contour intervals are for NO_3 every 2 mmol m^{-3}; for ΔNO_3 at ±12, ±7, ±4, ±2, and ±0.5 mmol m^{-3}; for NF every 0.05 mol m^{-2} yr^{-1}; for ΔNF at ±0.3, ±0.2, ±0.1, and ±0.05 mol m^{-2} yr^{-1}; for WCD at 0.05, 0.1, 0.3, 0.5, and 1 mol m^{-2} yr^{-1}; and for ΔWCD at ±1, ±0.3, ±0.2, ±0.1, and ±0.05 mol m^{-2} yr^{-1}.

3.2.6. Nitrogen Cycle

WCD is very sensitive to oxygen concentrations in the thermocline and thus shows variations by an order of magnitude across the different simulations (Table 1 and Figure 8). In model LGM0.6 WCD is decreased virtually everywhere (Figure 9) due to the shrunken suboxic zones. Increasing suboxic volumes in models with higher μ_{max}, however, increases WCD in the Pacific and Indian Oceans, whereas in the Atlantic it does not increase. Model LGM0.8 exhibits WCD in a few grid points in the Sea of Japan, which expands in LGM1.0, in which large additional areas in the subarctic North Pacific experience WCD. BD, on the other hand, is similar for all models and varies much less than WCD and NF, since it is mostly determined by the flux of organic carbon into the sediments and we did not consider the effect of sea level lowering.

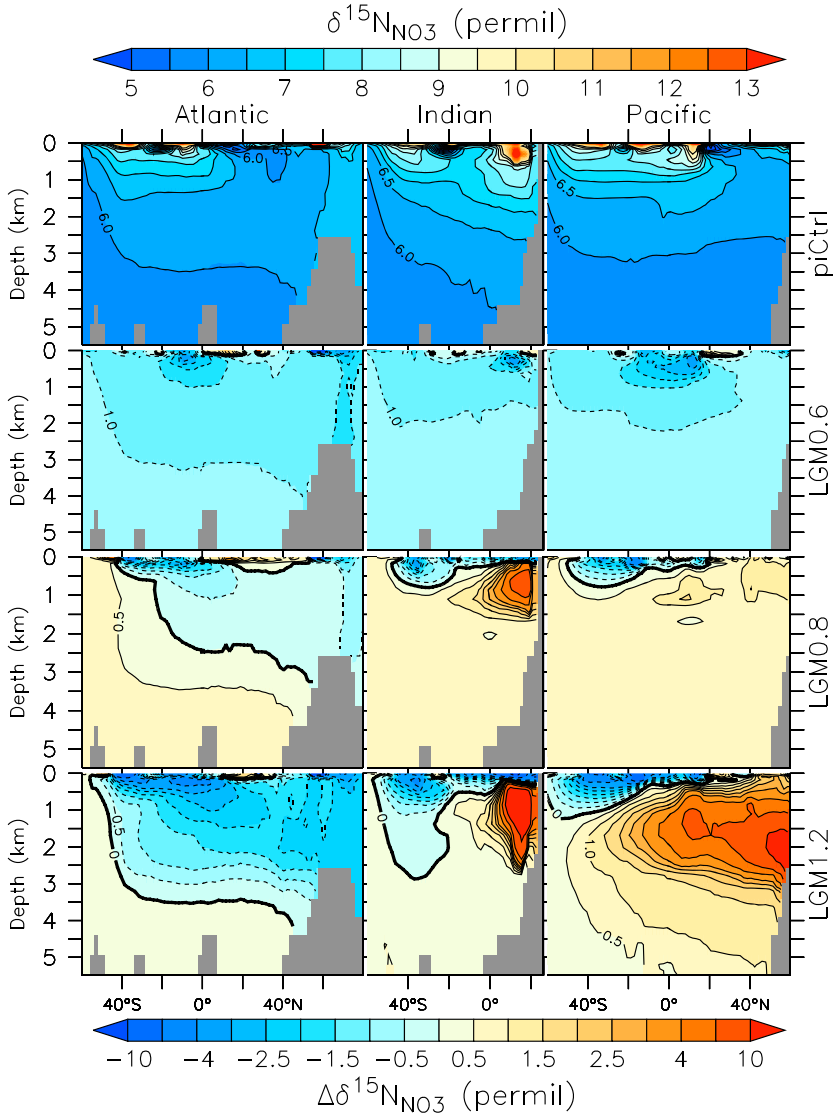

Figure 10. Zonally averaged distributions of (first row) $\delta^{15}N_{NO3}$ in piCtrl (top color bar) in the (left) Atlantic, (middle) Indian, and (right) Pacific. (second to fourth rows) $\delta^{15}N_{NO3}$ changes (LGM–piCtrl; bottom color bar) for three models as indicated at the right margin. Note that the color scale for $\Delta\delta^{15}N_{NO3}$ is linear between ±2.5 with an increment of 0.5‰ and nonlinear outside of that range with intervals at ±3, ±4, ±6, and ±10‰.

As the models approach equilibrium the global input of fixed nitrogen approximates the loss due to denitrification. Global NF varies by a factor of 5 ranging from 83 Tg/yr in LGM0.6 to 334 Tg/yr in LGM1.2 in response to changes in WCD (Table 1). NF is reduced everywhere in LGM0.6 compared to piCtrl (Figure 9). However, increasing WCD in the other LGM experiments leads to more NF particularly in the northern Indian Ocean and in a "C"-shaped area surrounding the eastern equatorial Pacific high nitrate waters stretching from around 15°N in the eastern and central Pacific to the equator in the tropical west Pacific and back east in a southeasterly direction around 20°S toward the west coast of South America because those regions are downstream of the increased WCD zones.

Zonally averaged surface nitrate concentrations are similar in LGM0.6 and piCtrl (Figure 8) although regionally larger changes appear (Figure 9) such as increases in the sea ice-covered Nordic Seas, subarctic North Pacific, and subantarctic Atlantic and Indian Ocean sectors of the Southern Ocean. Increases can also be observed in the eastern equatorial Pacific, whereas lower values appear in the North Atlantic south of the Nordic Seas, in the subantarctic eastern Pacific, and in parts of the tropical Atlantic and warm pool region

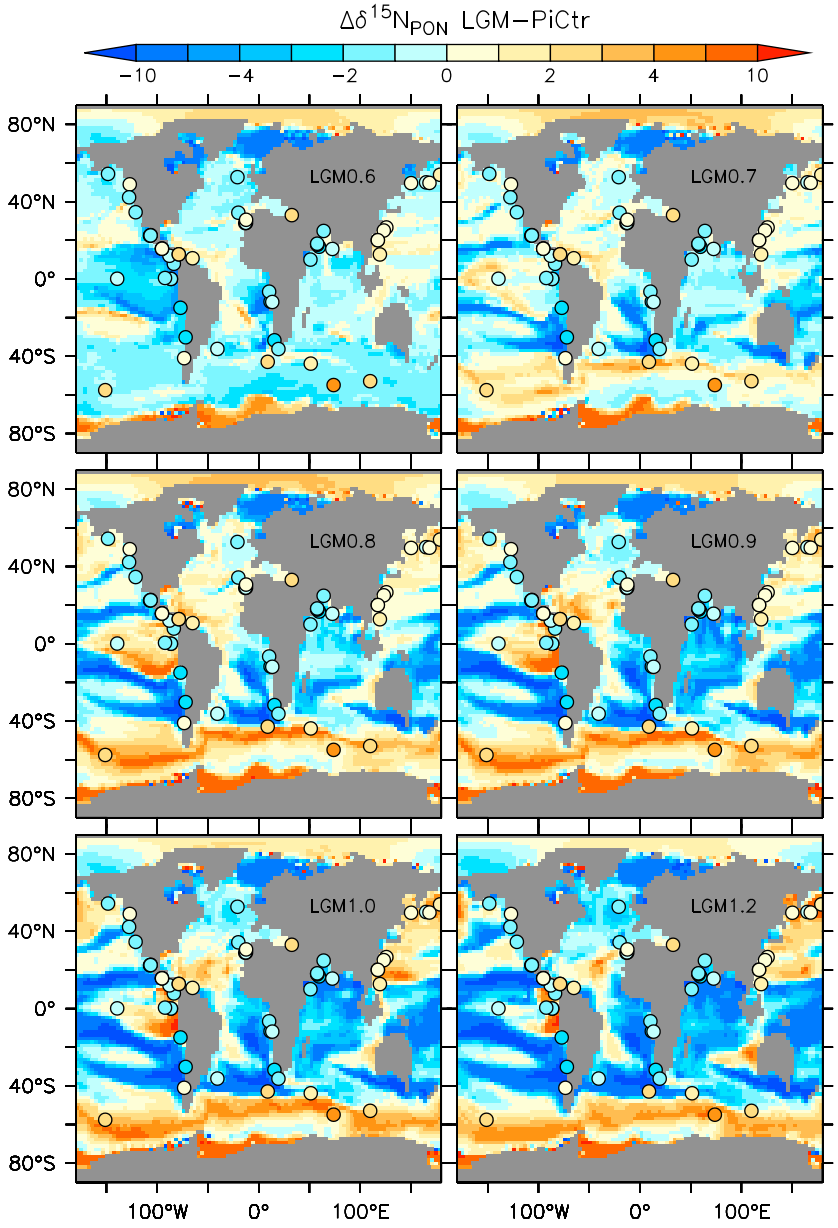

Figure 11. Changes (LGM–piCtrl) of $\delta^{15}N_{PON}$ in sinking particulate organic matter as simulated by the different models (color shadings) compared with observations (circles shaded using the same color scale).

of the eastern Indian/West Pacific. Some of the decreases in the tropics are colocated with and seem to be caused by reduced nitrogen fixation. Increasing nutrient utilization in the larger μ_{max} experiments lowers surface NO_3 almost everywhere in experiments LGM0.7 through LGM1.2, except under some sea ice-covered subpolar regions.

3.2.7. Nitrogen Isotopes

Model piCtrl shows values lower than 6‰ in the deepest layers of all ocean basins (Figure 10). The surface oceans in the subtropical gyres show high values due to fractionation during photosynthesis, and some regions in the tropical subsurface show high values due to WCD.

In model LGM0.6 surface $\delta^{15}N_{NO3}$ is lower almost everywhere compared with piCtrl (Figure 8) due to reduced WCD. Cross sections through the different ocean basins (Figure 10) illustrate how the signal that originates in the tropical thermocline spreads throughout the ocean all the way to high latitudes and great depths.

Table 2. Statistics From the Model-Data Comparison[a]

	δ^{15}N (LGM–piCtrl) $N = 45$					δ^{13}C (LGM) $N = 365$				
	R	RMSE	RMSE′	STDR	Bias	*R*	RMSE	RMSE′	STDR	Bias
piCtrl						0.63	1.48	0.79	0.78	0.66
LGM0.6	0.33	2.1	1.8	1.9	−1.5	0.75	1.14	**0.67**	0.80	0.59
LGM0.7	**0.45**	**1.3**	**1.2**	**1.3**	**−0.3**	0.77	0.87	**0.67**	0.95	0.29
LGM0.8	0.34	1.8	1.8	1.8	**−0.3**	**0.78**	0.76	0.69	**1.07**	0.17
LGM0.9	0.21	2.4	2.4	2.4	−0.8	**0.78**	**0.74**	0.72	1.14	0.09
LGM1.0	0.21	2.9	2.8	2.8	−1.2	**0.78**	0.75	0.75	1.19	**0.03**
LGM1.2	0.21	3.2	2.9	2.9	−2.1	**0.78**	0.77	0.78	1.25	**−0.03**

[a]Given are the number of data points (*N*), the correlation coefficient (*R*), the root-mean-square error normalized by the standard deviation of the observations (RMSE), RMSE of the anomalies from the mean (RMSE′), the ratio of standard deviations of the model over the observations (STDR), and the model mean minus that of the observations (bias in ‰). High values of *R*; low values of RMSE, RMSE′, and bias; and values close to 1 for STDR indicate good agreement. Best fits are indicated in bold.

Modeled differences in $\delta^{15}N_{PON}$ of particulate organic nitrogen between LGM0.6 and piCtrl reflect these decreases in $\delta^{15}N_{NO3}$ (Figure 11). The large decreases of $\delta^{15}N_{NO3}$ and $\delta^{15}N_{PON}$ in the Nordic Seas are due to more sea ice cover there, leading to lower productivity and nutrient utilization (Figure 9). Increases around 20° latitude in both hemispheres in the central and western tropical Pacific and Atlantic are caused by a reduction in NF in these regions (Figure 9).

At high latitudes the spatial distribution of $\delta^{15}N_{NO3}$ is dominated by fractionation due to the preferential uptake of isotopically light nitrogen by phytoplankton during photosynthesis [*Sigman et al.*, 1999; *Somes et al.*, 2010]. Thus, higher rates of nutrient utilization would be expected to increase $\delta^{15}N_{NO3}$ of surface nitrate there. This effect is indeed borne out in models LGM0.6 through LGM0.8 (Figures 8–11). However, further increases in phytoplankton growth rates lead to *decreases* in $\delta^{15}N_{NO3}$ of surface nitrate at high latitudes (Figure 8), contrary to the expectations from nutrient utilization. What could be the reason for this surprising result?

Since NF introduces isotopically light nitrate into the surface of the low-latitude oceans, $\delta^{15}N_{NO3}$ decreases there in models with higher μ_{max} and NF rates. The circulation of the upper ocean transports this isotopically light $\delta^{15}N_{NO3}$ toward higher latitudes. This effect, which is consistent with earlier results [*Somes et al.*, 2010, Figure 3], explains the $\delta^{15}N_{NO3}$ decreases at high latitudes for models LGM0.8 through LGM1.2.

Models with higher μ_{max} exhibit large increases of $\delta^{15}N_{NO3}$ in the Indian and Pacific Oceans' oxygen minimum zones, where WCD increases (Figure 10). Increased NF in these models leads to decreases in $\delta^{15}N_{PON}$ in a C-shaped arc around the eastern equatorial Pacific high nitrate waters, in the South Atlantic and in the Indian Ocean (Figure 9). Enhanced sources and sinks in models with high μ_{max} (Table 1) increase the spatial variance of the nitrogen isotopes such that the standard deviation increases from just 30% larger than the observations in model LGM0.7 to almost three times as large in model LGM1.2 (Table 2).

Higher $\delta^{15}N_{PON}$ values simulated in the eastern equatorial Pacific, in the equatorial North Atlantic and at high latitudes in the North Pacific and Southern Ocean, are impacted strongly by accelerated planktonic nutrient uptake and WCD as suggested by colocated decreases in surface nitrate and upstream increases in WCD (Figure 9).

3.2.8. Comparing Modeled Carbon Isotopes With Reconstructions

In the observations LGM $\delta^{13}C_{DIC}$ shows highest values of ~+1‰ in the North Atlantic and lowest values of ~−1‰ in the South Atlantic (Figure 12). This distribution is different from the modern observed distribution of bottom waters [*Schmittner et al.*, 2013] and those simulated by model piCtrl, which show high values throughout the Atlantic and lowest values of ~−0.4 ‰ in the North Pacific. Model LGM0.6 leads to somewhat lower values in the Atlantic compared with piCtrl, but $\delta^{13}C_{DIC}$ values everywhere outside of the North Atlantic are higher than those in the reconstructions. However, correlation coefficients and RMSE are significantly improved compared with piCtrl (Table 2) indicating the importance of circulation changes for $\delta^{13}C_{DIC}$ distributions. Increasing phytoplankton growth rates (LGM0.8–LGM1.2) decreases bottom water $\delta^{13}C_{DIC}$ values and further improves the agreement with the observations.

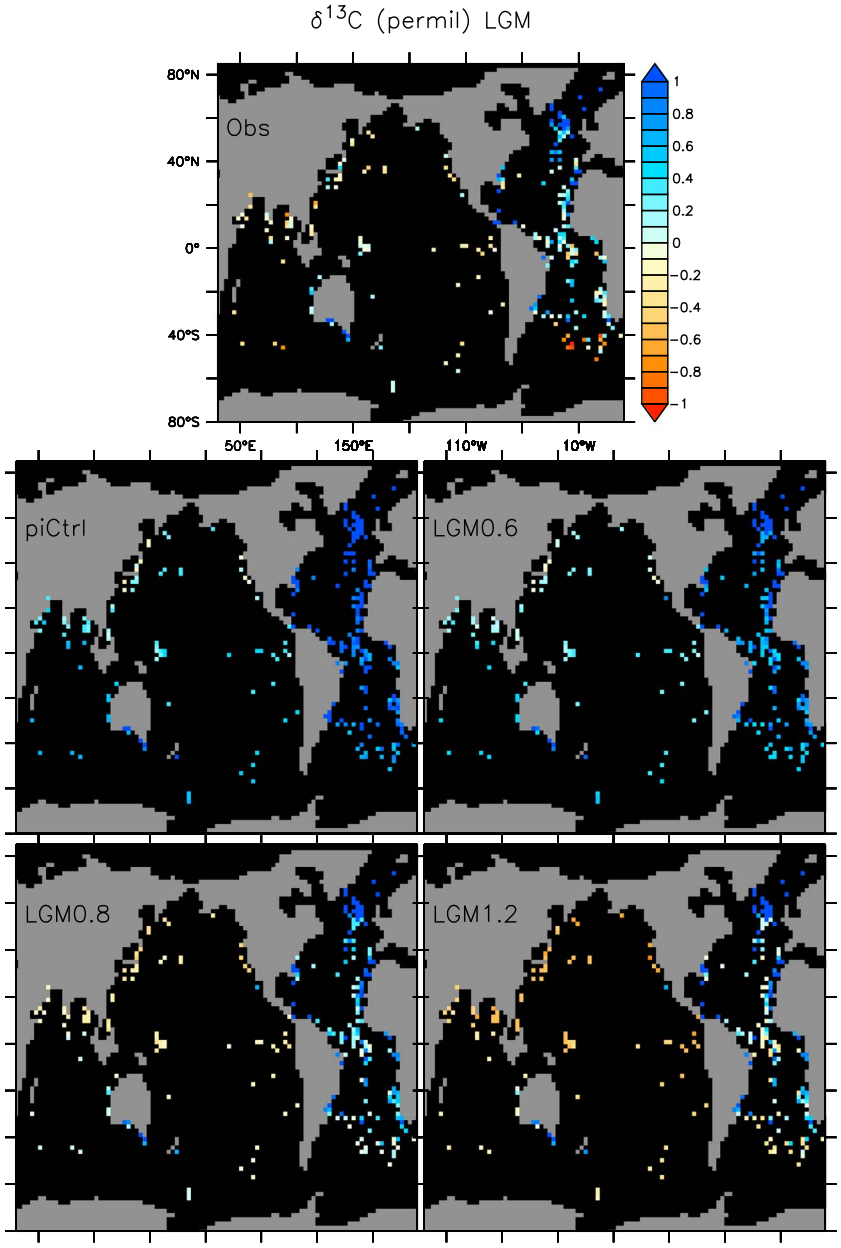

Figure 12. Maps of (top) LGM $\delta^{13}C_{DIC}$ from observations [*Peterson et al.*, 2014] interpolated on the model grid and (middle and bottom rows) four model simulations showing only those grid points where observations are available. Most locations only have one vertical grid box with observations but some have more, in which case the vertical average is shown.

However, none of our models is able to reproduce the minimum $\delta^{13}C_{DIC}$ values found in South Atlantic reconstructions.

Figure 13 shows that models with the highest growth rates (LGM1.0 and LGM1.2) agree best with basin-wide reconstructions in the Atlantic, Southern, and deep Indian Oceans, whereas the observations from the Pacific and upper Indian Oceans would favor models with moderately increased growth rate (LGM0.7 and LGM0.8). Global statistics (Table 2) and scatterplots (Figure 14) favor models with moderately increased growth rates. The RMSE is smallest and the correlation coefficient largest for model LGM0.9, whereas bias corrected RMS errors (RMSE') and STDR would favor models LGM0.7 and LGM0.8.

Figure 15 illustrates that model LGM0.8 captures the main, large-scale features of the observed LGM $\delta^{13}C_{DIC}$ distribution, such as large vertical gradients in the deep Atlantic with high values in the North Atlantic above

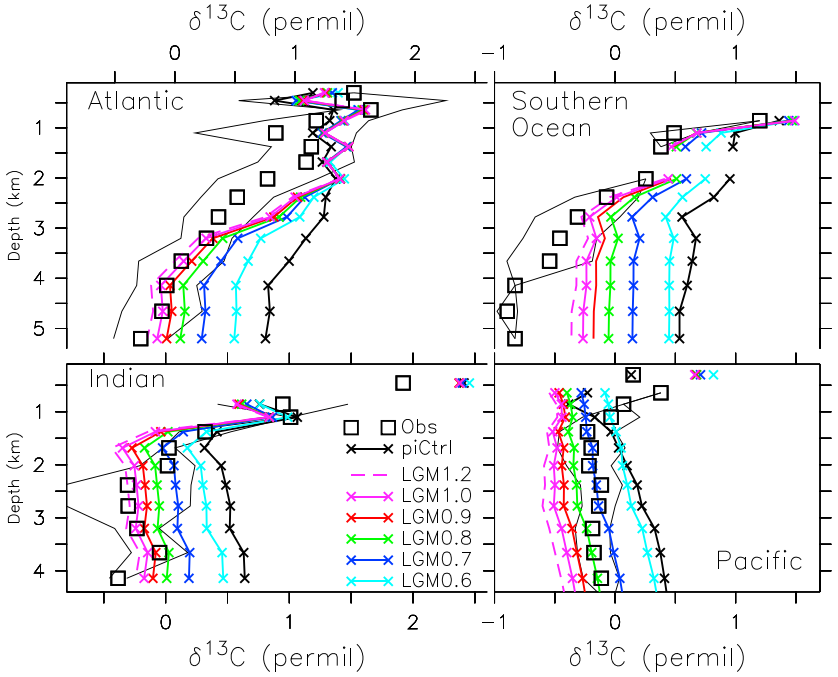

Figure 13. Horizontally averaged profiles of $\delta^{13}C_{DIC}$ in the different ocean basins. Square symbols indicate reconstructions from sediment cores (thin lines show 1σ standard deviations indicating spatial variability within each basin). Results from model simulations, sampled only in grid boxes where observations are available,are shown as x symbols and thick solid lines. The Southern Ocean is defined as south of 40°S.

2–3 km depth and low values in the deep South Atlantic, and more homogenous values in the deep Pacific and Indian Oceans. However, the model cannot reproduce the extremely low values suggested by the reconstructions in the South Atlantic south or 40°S and similarly low values in the deep Indian Ocean south of 40°S and north of 10°N. North Atlantic values at middepth are also overestimated by the model indicating a too strong and deep AMOC. Globally, model LGM0.8 overestimates $\delta^{13}C_{DIC}$ by 0.17‰ (Table 2).

3.2.9. Comparing Modeled Nitrogen Isotopes With Reconstructions

$\delta^{15}N$ records from LGM sediments document lower values in modern oxygen minimum zones such as the eastern equatorial Pacific and in the Arabian Sea indicating less WCD, higher values in the western tropics of the North Pacific and North Atlantic indicating less NF, and higher values in the Southern Ocean indicating enhanced nitrate utilization (Figure 11). Model LGM0.6 is consistent with the observed decreases of $\delta^{15}N_{PON}$ in the eastern and central Pacific north of 40°S; decreases observed in the South Atlantic, midlatitude North Atlantic, and in the Arabian Sea; and increases in the Caribbean. However, it is inconsistent with observed increases in the Southern Ocean and northeast Pacific. Models with moderately faster μ_{max} improve agreement with Southern Ocean and northeast Pacific observations. However, models with very high μ_{max} display large regions with extremely large values and others with unrealistically low $\delta^{15}N_{PON}$ values.

Mapping the observations onto the model grid and plotting modeled versus observed changes (Figure 14) illustrate the excessive increase in variance for high μ_{max} models. Whereas in the subpolar Southern Ocean and North Pacific values increase due to increased nutrient utilization, those in the tropical Arabian and Caribbean Seas decrease due to increased nitrogen fixation. Together with the analysis of standard statistical parameters (Table 2), this figure indicates that models with moderately increased growth rates (LGM0.7 and LGM0.8) fit the observations best.

4. Discussion

Carbon and nitrogen isotope reconstructions consistently favor LGM simulations with increased μ_{max} compared to modern. Global statistics (Table 2) suggest that nitrogen isotopes unambiguously favor model LGM0.7, with LGM0.8 coming in second place, whereas carbon isotopes are more ambiguous such that *R*,

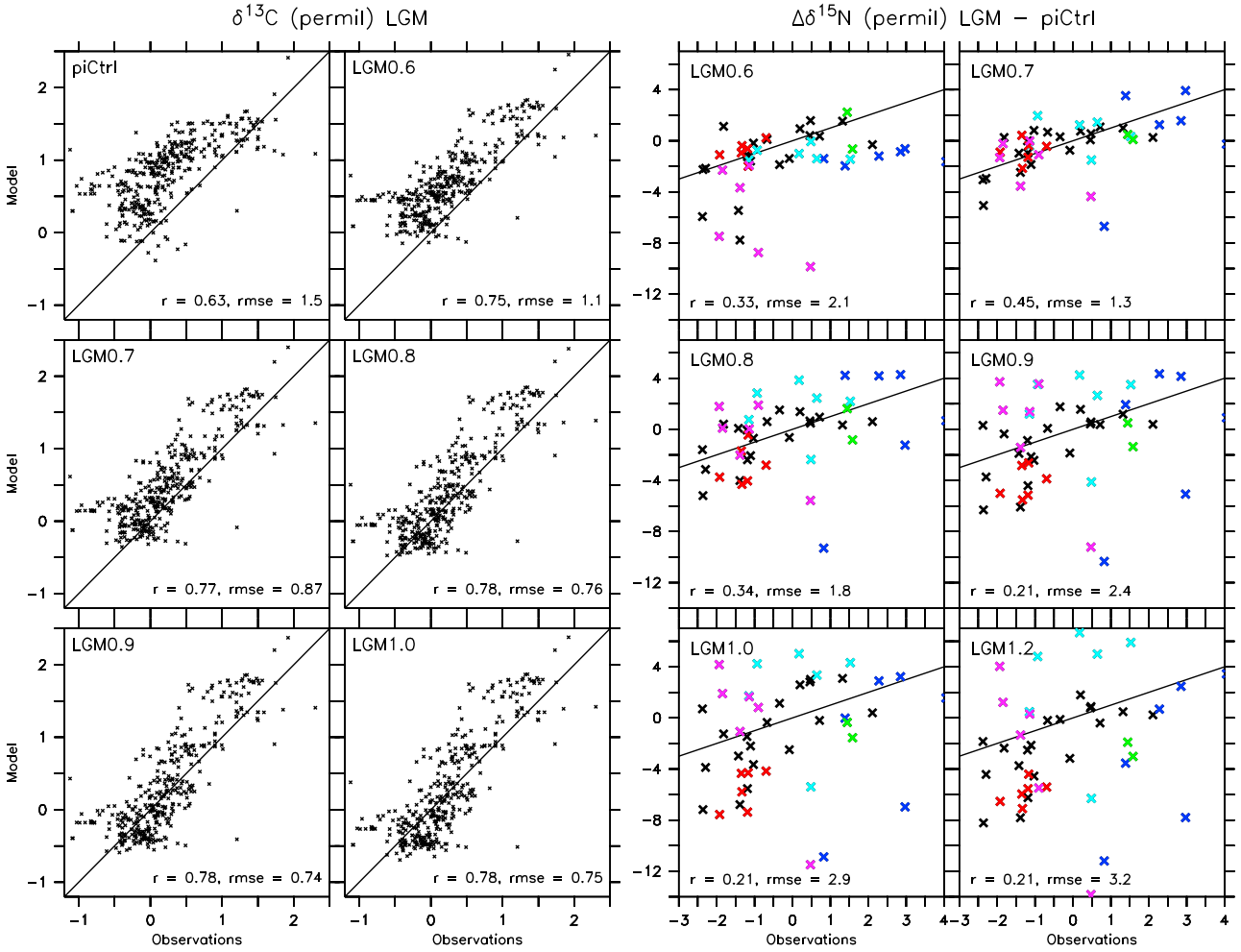

Figure 14. Observed versus modeled (left) carbon (LGM) and (right) nitrogen (LGM-LH; LH indicates late Holocene or piCtrl) isotopes. The one-to-one line indicates a perfect match. Colors indicate data from different regions. Blue: Southern Ocean south of 40°N, light blue: North Pacific 45°N–60°N, red: Arabian Sea, purple: eastern equatorial Pacific (120°W–85°W, 5°S–25°N), and green: Caribbean.

RMSE, and bias favor $\mu_{max} > 0.8$ and RMSE′ and STDR favor $\mu_{max} \leq 0.8$. Recognizing the ambiguity, we suggest that model LGM0.8 may be most consistent with the observations since most of its statistical parameters are close to those of the best fitting model, but a small positive bias remains. Although nitrogen isotopes favor slightly smaller increase in μ_{max} than carbon isotopes, both agree on a similar range $0.7 \leq \mu_{max} \leq 0.8$. Considering the idealized experimental setup and the model's simplifications, this agreement encourages further exploration of more realistic experiments.

Compared with the piCtrl export and primary production are decreased by 5–7% and 25% in the best fitting models LGM0.7 and LGM0.8, respectively, whereas in the default model LGM0.6 EP has decreased more (by 11%) and PP has decreased less (by 20%). Model LGM0.7, which best fits the nitrogen isotopes, indicates a ~20% decrease in WCD compared with piCtrl. This is less than the ~30–120% decrease estimated based on a global compilation on nitrogen isotopes that suggests a relatively constant global mean $\delta^{15}N_{NO3}$ and a sea level-based reconstruction of benthic denitrification [*Galbraith et al.*, 2013]. Overestimating carbon pump efficiency in the tropics by using a spatially constant increase in μ_{max} in the model may lead to excessive oxygen consumption and WCD there.

The inability of the best fitting models to reproduce all of the spatial patterns of $\delta^{13}C$ and $\delta^{15}N$ reconstructions suggests that future model versions should account for the spatial patterns of changes in soluble iron fluxes. Dust deposition estimates from the LGM suggest that almost all regions received more dust, but in some regions increase has been less (e.g., the tropical Indian and central Pacific) than elsewhere [*Lambert*

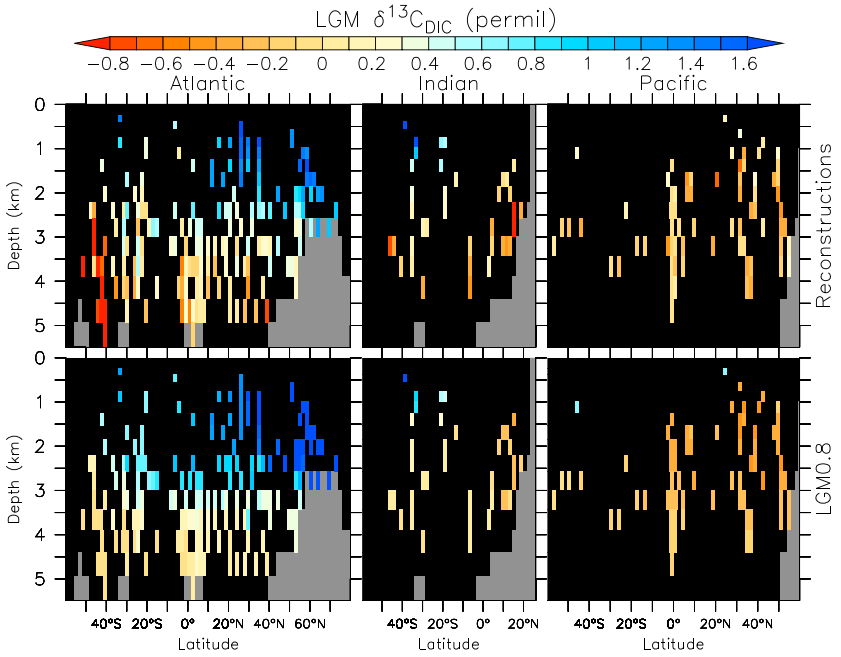

Figure 15. Zonally averaged $\delta^{13}C_{DIC}$ in the different ocean basins from the (top row) reconstructions and (bottom row) model LGM0.8 sampled at the location of the reconstructions.

et al., 2015]. Moreover, the effects of increased iron input on carbon drawdown will be higher in regions with abundant macronutrients that are iron limited, such as the Southern Ocean. Including the spatial patterns of iron input more realistically could improve some of the remaining biases in the $\delta^{13}C$ simulations such as overestimates in the Southern Ocean and underestimates in the Indian and Pacific Oceans. It could also improve the $\delta^{15}N$ simulations that overestimate the variance in the tropics presumably due to too much productivity fueling larger suboxic zones and enhanced WCD and NF. This highlights the advantage of using spatially resolving models that can be directly compared to observations to better indicate which processes need to be improved in the model.

Our assessment allows a first, albeit preliminary, data constrained quantification of C_{org} for the LGM. The best fitting models (LGM0.7 and LGM0.8) have a 590–790 Pg C (33–44%) larger C_{org} inventory than piCtrl. This suggests that more respired organic carbon was stored in the glacial ocean and that its soft-tissue pump was more efficient than during the late Holocene.

In order to properly estimate the consequences on whole ocean alkalinity (ALK), an interactive sediment model would be needed. Previous studies suggest that increased organic carbon storage in the deep ocean leads to dissolution of $CaCO_3$ from sediments and increases in whole ocean alkalinity, which would increase the preformed carbon inventory [*Broecker and Peng*, 1987; *Boyle*, 1988; *Brovkin et al.*, 2007; *Hain et al.*, 2010; *Ikeda and Tajika*, 2003; *Omta et al.*, 2013; *Sigman et al.*, 2010; *Toggweiler*, 1999]. Thus, including this effect would bring the total carbon inventories of our best fitting models in closer agreement with estimates from the global carbon isotope balance.

Many caveats exist in the model. Its atmospheric component is simplified, without three-dimensional dynamics. Its coarse resolution prevents accurate representation of smaller-scale processes such as mesoscale eddies or flow of Antarctic shelf water down the continental slope [*Hallberg and Gnanadesikan*, 2006; *Padman et al.*, 2009] although it has skill in simulating tracers such as chlorofluorocarbons or radiocarbon in the Southern Ocean [*Saenko et al.*, 2002; *Schmittner et al.*, 2008]. The inability of the model to fully reproduce the abyssal salinification (Figure S1) might be related to these deficiencies. However, since the purpose of our work is to examine the effects of the biological pump on nitrogen and carbon isotopes, accurate representation of these processes may not be crucial to our conclusions. In fact, the ability of the model to reproduce the major features of the glacial carbon isotope distribution indicates that resolving these processes may not be essential in order to capture the first-order changes between

glacial and interglacial circulations although the remaining biases (Figures 2 and 15) could be used to argue otherwise.

Another issue, which our model shares with other coarse resolution global ocean models, is the simulation of oxygen minimum zones, which are typically too weakly ventilated in the models [*Dietze and Loeptien*, 2013]. Simulated dissolved oxygen concentrations are therefore too low, suboxic regions are too large, WCD is overestimated, and nitrate values are underestimated. In MOBI these issues lead to one large suboxic zone in the eastern equatorial Pacific (Figure 9), whereas in reality two suboxic regions exist that are located farther away from the equator than in the model and those regions are separated by oxic waters along the equator. Other obvious issues are the displacement of suboxia in the Indian Ocean from the Arabian Sea, where they occur in the real ocean, to the Sea of Bengal in the model, as well as the simulation of suboxic regions in the equatorial Atlantic and in the Red Sea. Thus, the large increases of WCD simulated by the model for the high μ_{max} models may not be realistic, which would affect the nitrogen isotope model assessment.

Model LGM0.8, which arguably fits the carbon isotope reconstructions best, overestimates values in the deep Southern and Indian as well as in the intermediate North Atlantic Oceans (Figure 15) such that the whole ocean $\delta^{13}C_{DIC}$ is slightly overestimated (Table 2). The model's piCtrl simulation overestimates water column measurements of $\delta^{13}C_{DIC}$ in the intermediate North Atlantic and deep North Indian Oceans by ~0.3‰ [*Schmittner et al.*, 2013], which may explain similar overestimation in the LGM simulations there. Alternatively, these biases could indicate an overestimated AMOC. Modern biases in the Southern Ocean are negative and thus cannot explain the LGM differences with the reconstructions. Some benthic foraminiferal carbon isotope measurements have been shown to underestimate water column measurements of $\delta^{13}C_{DIC}$, a bias that has been attributed to organic phytodetritus layers that develop under strong seasonally varying productivity situations [*Mackensen et al.*, 2001, 1993], which may also influence the reconstructed extremely low values there, emphasizing that errors in the reconstructions need to be considered when interpreting model-data differences in this region.

Another potentially important neglection in our experiments is the effect of sea level lowering on BD, which should reduce nitrogen fixation and thus leads to generally higher $\delta^{15}N$ values. Neither did we consider spatially inhomogenous changes in growth rates. This will be possible in the future by using a model of iron cycling with spatially varying aeolian iron fluxes that is currently under development. Effects of iron and carbon fertilization on nitrogen fixers also remain to be explored [*Falkowski*, 1997].

All of our LGM simulations show lower oxygen concentrations in the deep ocean and higher oxygen concentrations in the upper thermocline compared with piCtrl (Figure 7), consistent, in general, with the differences between the LGM and the early Holocene sediment data as synthesized by *Jaccard and Galbraith* [2011, Figure 2]. If we assume that oxygen changes during the Holocene were relatively small compared to those between the LGM and early Holocene, we may infer that the increase in oxygen in the upper ocean in the models does not reach as deep as in the reconstructions, which suggest that the upper 1.5 km was better oxygenated, whereas in the model it is only the upper 0.5 to 1 km (Figure 7). This suggests that during the LGM more respired carbon was stored in the deep ocean and less in the intermediate ocean compared with the models. Deeper carbon storage would also decrease suboxia and WCD and bring models with a more efficient soft-tissue pump and lower $\delta^{13}C_{DIC}$ into better agreement with the nitrogen isotope observations. Deeper carbon storage could be accomplished by a more sluggish abyssal circulation and/or by biological processes such as faster particulate sinking speeds or slower remineralization rates.

5. Conclusions

Notwithstanding the above mentioned caveats we conclude that nitrogen and carbon isotopes provide complementary constraints on the glacial ocean's carbon cycle. Whereas carbon isotopes indicate the amount and distribution of biologically sequestered carbon in the deep ocean and are sensitive to circulation, nitrogen isotopes provide strong constraints on surface nutrient utilization, e.g., due to iron fertilization, nitrogen fixation, and denitrification. Here we have used both isotopes in combination, for the first time, in a global model-data comparison of the LGM. Our results support *Martin*'s [1990] hypothesis that increased iron input enhanced glacial ocean carbon storage by accelerating phytoplankton growth rates, consistent with previous studies [*Bopp et al.*, 2003; *Brovkin et al.*, 2007; *Tabliabue et al.*, 2009]. Our best fitting models suggest

that the amount of remineralized organic carbon in the glacial ocean was increased by 590–790 Pg and that both circulation and biology played important roles. However, these estimates are preliminary and subject to the caveats noted above. Improved estimates on atmospheric carbon drawdown will require more realistic model simulations with spatially variable changes of iron fluxes, consideration of sea level effects on BD, and interactive sediments. A systematic examination of circulation effects on both isotope distributions will be a useful complementary study to the one presented here.

Acknowledgments
Thanks to Carly Peterson for providing her carbon isotope compilation. We are greatly indebted to the many original producers of sedimentary carbon and nitrogen isotope data. This study was made possible by grant OCE-1131834 from the National Science Foundation's Marine Geology and Geophysics program. C.J.S was supported by the Deutsche Forschungsgemeinschaft via the SFB 754. We thank Eric Galbraith for constructive review comments. Data and model code used for this paper are available at the World Data Center for Paleoclimatology at the National Oceanic and Atmospheric Administration (https://www.ncdc.noaa.gov/paleo/study/19842).

References

Adkins, J. F., K. McIntyre, and D. P. Schrag (2002), The salinity, temperature, and $\delta^{18}O$ of the glacial deep ocean, *Science*, *298*(5599), 1769–1773, doi:10.1126/science.1076252.

Albani, S., N. M. Mahowald, A. T. Perry, R. A. Scanza, C. S. Zender, N. G. Heavens, V. Maggi, J. F. Kok, and B. L. Otto-Bliesner (2014), Improved dust representation in the Community Atmosphere Model, *J. Adv. Model. Earth Syst.*, *6*(3), 541–570, doi:10.1002/2013MS000279.

Altabet, M. A., M. J. Higginson, and D. W. Murray (2002), The effect of millennial-scale changes in Arabian Sea denitrification on atmospheric CO_2, *Nature*, *415*(6868), 159–162, doi:10.1038/415159a.

Annan, J. D., and J. C. Hargreaves (2013), A new global reconstruction of temperature changes at the Last Glacial Maximum, *Clim. Past*, *9*(1), 367–376, doi:10.5194/cp-9-367-2013.

Archer, D., A. Winguth, D. Lea, and N. Mahowald (2000), What caused the glacial/interglacial atmospheric pCO_2 cycles?, *Rev. Geophys.*, *38*(2), 159–189, doi:10.1029/1999RG000066.

Bohlen, L., A. W. Dale, and K. Wallmann (2012), Simple transfer functions for calculating benthic fixed nitrogen losses and C:N:P regeneration ratios in global biogeochemical models, *Global Biogeochem. Cycles*, *26*, GB3029, doi:10.1029/2011GB004198.

Bopp, L., K. E. Kohfeld, C. Le Quéré, and O. Aumont (2003), Dust impact on marine biota and atmospheric CO_2 during glacial periods, *Paleoceanography*, *18*(2), 1046, doi:10.1029/2002PA000810.

Bouttes, N., D. Paillard, D. M. Roche, V. Brovkin, and L. Bopp (2011), Last Glacial Maximum CO_2 and $\delta^{13}C$ successfully reconciled, *Geophys. Res. Lett.*, *38*, L02705, doi:10.1029/2010GL044499.

Boyle, E. A. (1988), Vertical oceanic nutrient fractionation and glacial/interglacial CO_2 cycles, *Nature*, *331*(6151), 55–56.

Brandes, J. A., and A. H. Devol (2002), A global marine-fixed nitrogen isotopic budget: Implications for Holocene nitrogen cycling, *Global Biogeochem. Cycles*, *16*(4), 1120, doi:10.1029/2001GB001856.

Broecker, W. S. (1982), Ocean chemistry during glacial time, *Geochim. Cosmochim. Acta*, *46*(10), 1689–1705.

Broecker, W. S., and G. M. Henderson (1998), The sequence of events surrounding Termination II and their implications for the cause of glacial-interglacial CO_2 changes, *Paleoceanography*, *13*(4), 352–364, doi:10.1029/98PA00920.

Broecker, W. S., and E. Maier-Reimer (1992), The influence of air and sea exchange on the carbon isotope distribution in the sea, *Global Biogeochem. Cycles*, *6*(3), 315–320, doi:10.1029/92GB01672.

Broecker, W. S., and T.-H. Peng (1987), The role of $CaCO_3$ compensation in the glacial to interglacial atmospheric CO_2 change, *Global Biogeochem. Cycles*, *1*(1), 15–29, doi:10.1029/GB001i001p00015.

Brovkin, V., M. Hofmann, J. Bendtsen, and A. Ganopolski (2002), Ocean biology could control atmospheric $\delta^{13}C$ during glacial-interglacial cycle, *Geochem. Geophys. Geosyst.*, *3*(5), 1027, doi:10.1029/2001GC000270.

Brovkin, V., A. Ganopolski, D. Archer, and S. Rahmstorf (2007), Lowering of glacial atmospheric CO_2 in response to changes in oceanic circulation and marine biogeochemistry, *Paleoceanography*, *22*, PA4202, doi:10.1029/2006PA001380.

Christensen, J. P. (1994), Carbon export from continental shelves, denitrification and atmospheric carbon dioxide, *Cont. Shelf Res.*, *14*(5), 547–576.

Ciais, P., et al. (2012), Large inert carbon pool in the terrestrial biosphere during the Last Glacial Maximum, *Nat. Geosci.*, *5*(1), 74–79, doi:10.1038/Ngeo1324.

Cline, J. D., and I. R. Kaplan (1975), Isotopic fractionation of dissolved nitrate during denitrification in the eastern tropical north pacific ocean, *Mar. Chem.*, *3*, 271–299, doi:10.1016/0304-4203(75)90009-2.

Curry, W. B., and D. W. Oppo (2005), Glacial water mass geometry and the distribution of $\delta^{13}C$ of ΣCO_2 in the western Atlantic Ocean, *Paleoceanography*, *20*, PA1017, doi:10.1029/2004PA001021.

Deutsch, C., D. M. Sigman, R. C. Thunell, A. N. Meckler, and G. H. Haug (2004), Isotopic constraints on glacial/interglacial changes in the oceanic nitrogen budget, *Global Biogeochem. Cycles*, *18*, GB4012, doi:10.1029/2003GB002189.

DeVries, T., C. Deutsch, P. A. Rafter, and F. Primeau (2013), Marine denitrification rates determined from a global 3-D inverse model, *Biogeosciences*, *10*(4), 2481–2496, doi:10.5194/bg-10-2481-2013.

Dietze, H., and U. Loeptien (2013), Revisiting "nutrient trapping" in global coupled biogeochemical ocean circulation models, *Global Biogeochem. Cycles*, *27*, 265–284, doi:10.1002/gbc.20029.

Duplessy, J. C., N. J. Shackleton, R. K. Matthews, W. Prell, W. F. Ruddiman, M. Caralp, and C. H. Hendy (1984), C-13 record of benthic foraminifera in the last interglacial ocean—Implications for the carbon-cycle and the global deep-water circulation, *Quaternary Res.*, *21*(2), 225–243.

Eugster, O., N. Gruber, C. Deutsch, S. L. Jaccard, and M. R. Payne (2013), The dynamics of the marine nitrogen cycle across the last deglaciation, *Paleoceanography*, *28*, 1–14, doi:10.1002/palo.20020.

Falkowski, P. G. (1997), Evolution of the nitrogen cycle and its influence on the biological sequestration of CO_2 in the ocean, *Nature*, *387*(6630), 272–275.

Galbraith, E. D., and S. L. Jaccard (2015), Deglacial weakening of the oceanic soft tissue pump: Global constraints from sedimentary nitrogen isotopes and oxygenation proxies, *Quaternary Sci. Rev.*, *109*, 38–48, doi:10.1016/j.quascirev.2014.11.012.

Galbraith, E. D., and A. C. Martiny (2015), A simple nutrient-dependence mechanism for predicting the stoichiometry of marine ecosystems, *Proc. Natl. Acad. Sci. U.S.A.*, *112*, 8199–8204, doi:10.1073/pnas.1423917112.

Galbraith, E. D., et al. (2013), The acceleration of oceanic denitrification during deglacial warming, *Nat. Geosci.*, *6*, 579–584, doi:10.1038/ngeo1832.

Galbraith, E. D., E. Y. Kwon, D. Bianchi, M. P. Hain, and J. L. Sarmiento (2015), The impact of atmospheric pCO_2 on carbon isotope ratios of the atmosphere and ocean, *Global Biogeochem. Cycles*, *29*, 307–324, doi:10.1002/2014GB004929.

Gebbie, G. (2014), How much did Glacial North Atlantic Water shoal?, *Paleoceanography*, *29*, 190–209, doi:10.1002/2013PA002557.
Hain, M. P., D. M. Sigman, and G. H. Haug (2010), Carbon dioxide effects of Antarctic stratification, North Atlantic Intermediate Water formation, and subantarctic nutrient drawdown during the last ice age: Diagnosis and synthesis in a geochemical box model, *Global Biogeochem. Cycles*, *24*, GB4023, doi:10.1029/2010GB003790.
Hallberg, R., and A. Gnanadesikan (2006), The role of eddies in determining the structure and response of the wind-driven southern hemisphere overturning: Results from the Modeling Eddies in the Southern Ocean (MESO) project, *J. Phys. Oceanogr.*, *36*(12), 2232–2252.
Hesse, T., D. Wolf-Gladrow, G. Lohmann, J. Bijma, A. Mackensen, and R. E. Zeebe (2014), Modelling delta C-13 in benthic foraminifera: Insights from model sensitivity experiments, *Mar. Micropaleontol.*, *112*, 50–61, doi:10.1016/j.marmicro.2014.08.001.
Ikeda, T., and E. Tajika (2003), Carbon cycling and climate change during the last glacial cycle inferred from the isotope records using an ocean biogeochemical carbon cycle model, *Global Planet. Change*, *35*, 131–141, doi:10.1016/S0921-8181(02)00134-0.
Insua, T. L., A. J. Spivack, D. Graham, S. D'Hondt, and K. Moran (2014), Reconstruction of Pacific Ocean bottom water salinity during the Last Glacial Maximum, *Geophys. Res. Lett.*, *41*, 2914–2920, doi:10.1002/2014GL059575.
Jaccard, S. L., and E. D. Galbraith (2011), Large climate-driven changes of oceanic oxygen concentrations during the last deglaciation, *Nat. Geosci.*, *5*(2), 151–156, doi:10.1038/ngeo1352.
Kalnay, E., et al. (1996), The NCEP/NCAR 40-year reanalysis project, *Bull. Am. Meteorol. Soc.*, *77*(3), 437–471.
Knox, F., and M. B. McElroy (1984), Changes in atmospheric CO_2: Influence of the marine biota at high latitude, *J. Geophys. Res.*, *89*(D3), 4629–4637, doi:10.1029/JD089iD03p04629.
Köhler, P., H. Fischer, and J. Schmitt (2010), Atmospheric $\delta^{13}CO_2$ and its relation to pCO_2 and deep ocean $\delta^{13}C$ during the late Pleistocene *Paleoceanography*, *25*, PA1213, doi:10.1029/2008PA001703.
Lambert, F., A. Tagliabue, G. Shaffer, F. Lamy, G. Winckler, L. Farias, L. Gallardo, and R. De Pol-Holz (2015), Dust fluxes and iron fertilization in Holocene and Last Glacial Maximum climates, *Geophys. Res. Lett.*, *42*, 6014–6023, doi:10.1002/2015GL064250.
Lehmann, M. F., D. M. Sigman, D. C. McCorkle, J. Granger, S. Hoffmann, G. Cane, and B. G. Brunelle (2007), The distribution of nitrate 15 N/14 N in marine sediments and the impact of benthic nitrogen loss on the isotopic composition of oceanic nitrate, *Geochim. Cosmochim. Acta*, *71*(22), 5384–5404, doi:10.1016/j.gca.2007.07.025.
Mackensen, A., M. Rudolph, and G. Kuhn (2001), Late Pleistocene deep-water circulation in the subantarctic eastern Atlantic, *Global Planet. Change*, *30*(3–4), 197–229.
Mahowald, N. M., D. R. Muhs, S. Levis, P. J. Rasch, M. Yoshioka, C. S. Zender, and C. Luo (2006), Change in atmospheric mineral aerosols in response to climate: Last glacial period, preindustrial, modern, and doubled carbon dioxide climates, *J. Geophys. Res.*, *111*, D10202, doi:10.1029/2005JD006653.
Mahowald, N. M., et al. (2009), Atmospheric iron deposition: Global distribution, variability, and human perturbations, *Annu. Rev. Mar. Sci.*, *1*, 245–278, doi:10.1146/annurev.marine.010908.163727.
Marcott, S. A., et al. (2014), Centennial-scale changes in the global carbon cycle during the last deglaciation, *Nature*, *514*(7524), 616–619, doi:10.1038/Nature13799.
Martin, J. H. (1990), Glacial-interglacial CO_2 change: The Iron Hypothesis, *Paleoceanography*, *5*(1), 1–13, doi:10.1029/PA005i001p00001.
Martinez-Garcia, A., D. M. Sigman, H. J. Ren, R. F. Anderson, M. Straub, D. A. Hodell, S. L. Jaccard, T. I. Eglinton, and G. H. Haug (2014), Iron fertilization of the subantarctic ocean during the last ice age, *Science*, *343*(6177), 1347–1350, doi:10.1126/science.1246848.
Matsumoto, K., T. Hashioka, and Y. Yamanaka (2007), Effect of temperature-dependent organic carbon decay on atmospheric pCO_2, *J. Geophys. Res.*, *112*, G02007, doi:10.1029/2006JG000187.
McElroy, M. B. (1983), Marine biological-controls on atmospheric CO_2 and climate, *Nature*, *302*(5906), 328–329.
Meissner, K. J., A. J. Weaver, H. D. Matthews, and P. M. Cox (2003), The role of land surface dynamics in glacial inception: A study with the UVic Earth System Model, *Clim. Dynam.*, *21*(7–8), 515–537, doi:10.1007/S00382-003-0352-2.
Meissner, K. J., E. D. Galbraith, and C. Völker, 2005: Denitrification under glacial and interglacial conditions: A physical approach, *Paleoceanography*, *20*, PA3001, doi:10.1029/2004PA001083.
Miller, M. D., M. Simons, J. F. Adkins, and S. E. Minson (2015), The information content of pore fluid $\delta^{18}O$ and $[Cl^-]$, *J. Phys. Oceanogr.*, *45*(8), 2070–2094, doi:10.1175/JPO-D-14-0203.1.
Minagawa, M., and E. Wada (1986), Nitrogen isotope ratios of red tide organisms in the East China Sea: A characterization of biological nitrogen fixation, *Mar. Chem.*, *19*, 245–259, doi:10.1016/0304-4203(86)90026-5.
Omta, A. W., G. A. K. van Voorn, R. E. Rickaby, and M. Follows (2013), On the potential role of marine calcifiers in glacial-interglacial dynamics, *Global Biogeochem. Cycles*, *27*, 692–704, doi:10.1002/gbc.20060.
Padman, L., S. L. Howard, A. H. Orsi, and R. D. Muench (2009), Tides of the northwestern Ross Sea and their impact on dense outflows of Antarctic Bottom Water, *Deep Sea Res. Part II*, *56*(13–14), 818–834, doi:10.1016/j.dsr2.2008.10.026.
Parek, P., M. J. Follows, and E. Boyle (2004), Modeling the global ocean iron cycle, *Global Biogeochem. Cycles*, *18*, GB1002, doi:10.1029/2003GB002061.
Parrenin, F., V. Masson-Delmotte, P. Köhler, D. Raynaud, D. Paillard, J. Schwander, C. Barbante, A. Landais, A. Wegner, and J. Jouzel (2013), Synchronous change of atmospheric CO_2 and Antarctic temperature during the last deglacial warming, *Science*, *339*(6123), 1060–1063, doi:10.1126/science.1226368.
Peterson, C. D., L. E. Lisiecki, and J. V. Stern (2014), Deglacial whole-ocean $\delta^{13}C$ change estimated from 480 benthic foraminiferal records, *Paleoceanography*, *29*, 549–563, doi:10.1002/2013PA002552.
Petit, J. R., et al. (1999), Climate and atmospheric history of the past 420,000 years from the Vostok ice core, Antarctica, *Nature*, *399*(6735), 429–436.
Redfield, A. C. (1958), The biological control of chemical factors in the environment, *Am. Sci.*, *46*(3), 205–221.
Ren, H., D. M. Sigman, A. N. Meckler, B. Plessen, R. S. Robinson, Y. Rosenthal, and G. H. Haug (2009), Foraminiferal isotope evidence of reduced nitrogen fixation in the ice age Atlantic Ocean, *Science*, *323*(5911), 244–248, doi:10.1126/science.1165787.
Ren, H., D. M. Sigman, M. T. Chen, and S. J. Kao (2012), Elevated foraminifera-bound nitrogen isotopic composition during the last ice age in the South China Sea and its global and regional implications, *Global Biogeochem. Cycles*, *26*, GB1031, doi:10.1029/2010GB004020.
Robinson, R. S., et al. (2012), A review of nitrogen isotopic alteration in marine sediments, *Paleoceanography*, *27*, PA4203, doi:10.1029/2012PA002321.
Roche, D. M., X. Crosta, and H. Renssen (2012), Evaluating Southern Ocean sea-ice for the Last Glacial Maximum and pre-industrial climates: PMIP-2 models and data evidence, *Quat. Sci. Rev.*, *56*, 99–106, doi:10.1016/j.quascirev.2012.09.020.
Saenko, O. A., A. Schmittner, and A. J. Weaver (2002), On the role of wind-driven sea ice motion on ocean ventilation, *J. Phys. Oceanogr.*, *32*(12), 3376–3395.

Sarmiento, J. L., and J. R. Toggweiler (1984), A new model for the role of the oceans in determining atmospheric pCO_2, *Nature*, *308*(5960), 621–624.
Sarnthein, M., B. Schneider, and P. M. Grootes (2013), Peak glacial ^{14}C ventilation ages suggest major draw-down of carbon into the abyssal ocean, *Clim. Past*, *9*(6), 2595–2614, doi:10.5194/cp-9-2595-2013.
Schmitt, J., et al. (2012), Carbon isotope constraints on the deglacial CO_2 rise from ice cores, *Science*, *336*(6082), 711–714, doi:10.1126/science.1217161.
Schmittner, A. (2003), Southern ocean sea ice and radiocarbon ages of glacial bottom waters, *Earth Planet. Sci. Lett.*, *213*(1–2), 53–62, doi:10.1016/S0012-821x(03)00291-7.
Schmittner, A. (2005), Decline of the marine ecosystem caused by a reduction in the Atlantic overturning circulation, *Nature*, *434*(7033), 628–633.
Schmittner, A., and D. C. Lund (2015), Early deglacial Atlantic overturning decline and its role in atmospheric CO_2 rise inferred from carbon isotopes ($\delta^{13}C$), *Clim. Past*, *11*(2), 135–152.
Schmittner, A., A. Oschlies, H. D. Matthews, and E. D. Galbraith (2008), Future changes in climate, ocean circulation, ecosystems, and biogeochemical cycling simulated for a business-as-usual CO_2 emission scenario until year 4000 AD, *Global Biogeochem. Cycles*, *22*, GB1013, doi:10.1029/2007GB002953.
Schmittner, A., N. Gruber, A. C. Mix, R. M. Key, A. Tagliabue, and T. K. Westberry (2013), Biology and air-sea gas exchange controls on the distribution of carbon isotope ratios ($\delta^{13}C$) in the ocean, *Biogeosciences*, *10*(9), 5793–5816.
Schmittner, A., J. A. M. Green, and S. B. Wilmes (2015), Glacial ocean overturning intensified by tidal mixing in a global circulation model, *Geophys. Res. Lett.*, *42*, 4014–4022, doi:10.1002/2015GL063561.
Shackleton, N. J. (1977), Carbon-13 in Uvigerina: Tropical rainforest history and the Equatorial Pacific carbonate dissolution cycles, in *The Fate of Fossil Fuel CO_2 in the Oceans*, edited by N. R. Andersen and A. Malahoff, pp. 401–427, Plenum, New York.
Shackleton, N. J., J. Le, A. Mix, and M. A. Hall (1992), Carbon isotope records from Pacific surface waters and atmospheric carbon-dioxide, *Quaternary Sci. Rev.*, *11*(4), 387–400.
Sigman, D. M., and E. A. Boyle (2000), Glacial/interglacial variations in atmospheric carbon dioxide, *Nature*, *407*(6806), 859–869.
Sigman, D. M., M. A. Altabet, D. C. McCorkle, R. Francois, and G. Fischer (1999), The delta N-15 of nitrate in the Southern Ocean: Consumption of nitrate in surface waters, *Global Biogeochem. Cycles*, *13*, 1149–1166, doi:10.1029/1999GB900038.
Sigman, D. M., M. P. Hain, and G. H. Haug (2010), The polar ocean and glacial cycles in atmospheric CO_2 concentration, *Nature*, *466*(7302), 47–55, doi:10.1038/Nature09149.
Skinner, L. C., S. Fallon, C. Waelbroeck, E. Michel, and S. Barker (2010), Ventilation of the deep Southern Ocean and deglacial CO2 rise, *Science*, *328*(5982), 1147–1151.
Somes, C. J., and A. Oschlies (2015), On the influence of "non-Redfield" dissolved organic nutrient dynamics on the spatial distribution of N_2 fixation and the size of the marine fixed nitrogen inventory, *Global Biogeochem. Cycles*, *29*, 973–993, doi:10.1002/2014GB005050.
Somes, C. J., A. Schmittner, E. D. Galbraith, M. F. Lehmann, M. A. Altabet, J. P. Montoya, R. M. Letelier, A. C. Mix, A. Bourbonnais, and M. Eby (2010), Simulating the global distribution of nitrogen isotopes in the ocean, *Global Biogeochem. Cycles*, *24*, GB4019, doi:10.1029/2009GB003767.
Somes, C. J., A. Oschlies, and A. Schmittner (2013), Isotopic constraints on the pre-industrial oceanic nitrogen budget, *Biogeosciences*, *10*(9), 5889–5910, doi:10.5194/bg-10-5889-2013.
Spero, H. J., J. Bijma, D. W. Lea, and B. E. Bemis (1997), Effect of seawater carbonate concentration on foraminiferal carbon and oxygen isotopes, *Nature*, *390*(6659), 497–500.
Straub, M., M. M. Tremblay, D. M. Sigman, A. S. Studer, H. Ren, J. R. Toggweiler, and G. H. Haug (2013), Nutrient conditions in the subpolar North Atlantic during the last glacial period reconstructed from foraminifera-bound nitrogen isotopes, *Paleoceanography*, *28*, 79–90, doi:10.1002/palo.20013.
Studer, A. S., et al. (2015), Antarctic zone nutrient conditions during the last two glacial cycles, *Paleoceanography*, *30*, 845–862, doi:10.1002/2014PA002745.
Tagliabue, A., L. Bopp, D. M. Roche, N. Bouttes, J. C. Dutay, R. Alkama, M. Kageyama, E. Michel, and D. Paillard (2009), Quantifying the roles of ocean circulation and biogeochemistry in governing ocean carbon-13 and atmospheric carbon dioxide at the last glacial maximum, *Clim. Past*, *5*, 695–706.
Toggweiler, J. R. (1999), Variation of atmospheric CO_2 by ventilation of the ocean's deepest water, *Paleoceanography*, *14*(5), 571–588, doi:10.1029/1999PA900033.
Volk, T., and M. I. Hoffert (1985), Ocean carbon pumps: Analysis of relative strengths and efficiencies in ocean-driven atmospheric CO_2 changes, in *The Carbon Cycle and Atmospheric CO_2: Natural Variations Archean to Present*, pp. 99–110, AGU, Washington, D. C.
Wada, E. (1980), Nitrogen isotope fractionation and its significance in biogeochemical processes occurring in marine environments, *Isotope Mar. Chem.*, *1*, 375–398.
Wallmann, K. (2014), Is late Quaternary climate change governed by self-sustained oscillations in atmospheric CO_2?, *Geochim. Cosmochim. Acta*, *132*, 413–439, doi:10.1016/j.gca.2013.10.046.
Wallmann, K., B. Schneider, and M. Sarnthein (2016), Effects of eustatic sea-level change, ocean dynamics, and nutrient utilization on atmospheric pCO_2 and seawater composition over the last 130 000 years: A model study, *Clim. Past*, *12*(2), 339–375, doi:10.5194/cp-12-339-2016.
Weaver, A. J., C. M. Bitz, A. F. Fanning, and M. M. Holland (1999), Thermohaline circulation: High-latitude phenomena and the difference between the Pacific and Atlantic, *Annu. Rev. Earth Planet. Sci.*, *27*, 231–285.
Weber, T. S., and C. Deutsch (2010), Ocean nutrient ratios governed by plankton biogeography, *Nature*, *467*, 550–554, doi:10.1038/nature09403.
Wunsch, C. (2016), Pore fluids and the LGM ocean salinity-reconsidered, *Quat. Sci. Rev.*, *135*, 154–170.
Zeebe, R. E., and D. A. Wolf-Gladrow (2001), *CO_2 in Seawater: Equilibrium, Kinetics, Isotopes*, Elsevier, Amsterdam.